SAND2004-5060
Unlimited Release
Printed October 2004

SOOT FORMATION, TRANSPORT, AND RADIATION IN UNSTEADY DIFFUSION FLAMES

LDRD Final Report

Christopher R. Shaddix, Timothy C. Williams,
Linda G. Blevins, and Robert W. Schefer

Combustion Research Facility
Sandia National Laboratories
Livermore, CA 94550

Kirk A. Jensen and Jill M. Suo-Antilla

Fire Science and Technology

and

Sean P. Kearney

Thermal/Fluid Experimental Sciences
Sandia National Laboratories
Albuquerque, NM 87185

Abstract

Fires pose the dominant risk to the safety and security of nuclear weapons, nuclear transport containers, and DOE and DoD facilities. The thermal hazard from these fires primarily results from radiant emission from high-temperature flame soot. Therefore, it is necessary to understand the local transport and chemical phenomena that determine the distributions of soot concentration, optical properties, and temperature in order to develop and validate constitutive models for large-scale, high-fidelity fire simulations. This report summarizes the findings of a Laboratory Directed Research and Development (LDRD) project devoted to obtaining the critical experimental information needed to develop such constitutive models. A combination of laser diagnostics and extractive measurement techniques have been employed in both steady and pulsed laminar diffusion flames of methane, ethylene, and JP-8 surrogate burning in air. For methane and ethylene, both slot and coannular flame geometries were investigated, as well as normal and inverse diffusion flame geometries. For the JP-8 surrogate, coannular normal diffusion flames were investigated. Soot concentrations, polycyclic aromatic hydrocarbon (PAH) laser-induced fluorescence (LIF) signals, hydroxyl radical (OH) LIF, acetylene and water vapor concentrations, soot zone temperatures, and the velocity field were all successfully measured in both steady and unsteady versions of these various flames. In addition, measurements were made of the soot microstructure, soot dimensionless extinction coefficient (K_e), and the local radiant heat flux. Taken together, these measurements comprise a unique, extensive database for future development and validation of models of soot formation, transport, and radiation.

This page intentionally left blank.

Table of Contents **Page**

Abstract 3

Table of Contents 5

List of Figures 6

List of Tables 10

Acknowledgments 11

Introduction 12

Overview of Soot and Radiation Modeling 12

Measurement Approach 13

Burner and Flame Specification 15

Burners and Flames 16

Wolfhard-Parker Burner 16

Gas Fuel Coannular Burner 19

Liquid Fuel Coannular Burner 21

Choice of Unsteady Flame Conditions 22

OH and PAH, Soot Radiation 24

Soot Volume Fraction 25

Velocity Field 27

Temperature 29

Acetylene and Water Vapor 30

Soot Dimensionless Extinction Coefficient 33

Soot Microstructure 37

Local Radiant Heat Flux 39

Conclusions 42

List of References 43

List of Figures

Figure 1. Photographs of Wolfhard-Parker burner (a) from the side of the slot, showing loudspeaker and chimney enclosure with optical access window and stabilizing screen, (b) looking down at the burner face with the chimney removed, and (c) looking down the axis of the slot with "gull wing" stabilization screens in view. 17

Figure 2. Schematic of Wolfhard-Parker burner with laser sheet and intensified CCD camera for flame imaging. 17

Figure 3. Schematic of Wolfhard-Parker burner with chimney extension and outlet screen for operation of inverse diffusion flames 18

Figure 4. Photographs of ethylene/air Wolfhard-Parker normal diffusion flames: (a) side-view of steady flame, with the bottom edge of the stabilization screen evident, (b, c) two different phases of the pulsed flame. 19

Figure 5. Photographs of investigated steady Wolfhard-Parker flames, showing (from left to right, for each fuel) a close-up of the NDF, a distant view of NDF, and a close-up of the IDF. 19

Figure 6. Photographs of coannular gas fuel burner (a) with chimney attached, showing optical access windows, (b) side profile, showing loudspeaker on burner base, and (c) looking down on the burner face, with ceramic honeycomb and central fuel tube 20

Figure 7. Photographs of steady methane, ethylene, and JP-8 surrogate coannular flames. 21

Figure 8. Photographs of (a) capillary force vaporizer, with fuel vapor jetting from central hole, (b) vaporizer unit attached to bottom of burner, with cooling fins and fan, (c) fuel tube, with coiled heater and sidearm connection, and (d) assembled burner, with model airplane piston attached to modulate fuel flow. 21

Figure 9. Schematic of pulsed slot burner and associated laser beam deflection and laser sheet imaging diagnostics. 23

Figure 10. Maps of flame response to fuel forcing frequency and amplitude for the methane and ethylene slot flames 24

Figure 11. ICCD images (50-mm high) of simultaneously excited OH PLIF and PAH PLIF. The top two rows show images of the steady and 15 Hz pulsed methane and ethylene slot flames. The last row shows images of the steady and 15 Hz pulsed JP-8 surrogate/N_2 coannular flames. Soot LII signals are weakly evident as thin streaks in the pulsed ethylene flames and are strong signals in upper regions of the JP-8 flame. 26

Figure 12. ICCD images (50-mm high) of 850 nm (thermal) emission from the 15 Hz pulsed ethylene slot flame. The phases shown here correspond to the first 5 phases shown for PLIF imaging of this flame in Fig. 11. 27

Figure 13. Stacked, planar images of LII from the steady and 15 Hz pulsed methane coannular flame. 27

Figure 14. Overlay of ICCD image of (a) light scattering from heavily seeded airflow and (b) velocity vectors, obtained by performing PIV on lightly seeded fuel and air flows. The flow exiting the fuel slot appears dark. 28

Figure 15. Lower images: overlay of OH/PAH PLIF image and air-side velocity field from the 15 Hz ethylene slot flame for three successive phase increments of 20°. The mean vertical velocity on the air-side of the flame sheet has been subtracted from each of the images to clearly show the embedded vortex structure. Upper images: false color PLIF images, with the regions interrogated in the lower images indicated by squares. 28

Figure 16. Photograph of 2-color pyrometry imaging setup. 29

Figure 17. Photograph of filtered Rayleigh scattering diagnostic setup for wavelength scanning and locking of an injection-seeded YAG. The horizontal cylinder on the left is an iodine cell 30

Figure 18. Photograph of TDLAS electronics setup: laser temperature controller to the left; function generators and lock-in amplifier electronics to the right. 31

Figure 19. Linestrengths and line centers of water and acetylene absorption features within the tuning range of the diode laser used to measure acetylene. HiTran data is used for all but the high-temperature acetylene line strengths, which were derived from earlier spectral modeling (Shaddix et al., 2001). The temperatures indicate the laser control temperature used to produce laser light that is resonant with the indicated acetylene transition. 31

Figure 20. Photographs of TDLAS optical configuration, with (a) fiber pigtailed collimator within window-sealed body, (b) canted optical flat attached to window-sealed body, and (c) focusing mirror, bandpass filter, and diode detector, downstream of optical flat.....32

Figure 21. Example of a single 250 Hz ramp scan of a water absorption line at a height of 20 mm and a transverse position of 10 mm from the centerline of the steady ethylene slot flame. The two "2f" signals shown here are in a quadrature phase relationship.....32

Figure 22. Schematic and photograph of quartz microprobe, constructed for unobtrusive soot sampling from laminar flames.....33

Figure 23. Photographs showing (a) equipment rack with flow controllers, valves, and filter assemblies for controlling operation of the TCRN, (b) soot transport and dilution line, leading from the flame, and (c) stainless steel sampling probe, drawing soot from the ethylene slot flame. 34

Figure 24. Time record of laser transmission signals from the TCRN diagnostic when sampling from the steady ethylene slot flame at a height of 65 mm. The plateau regions at the beginning and end of the time record denote the baseline laser transmission when the probe is sampling clean air. The two rapid drops in transmission in the middle of the sampling period follow probe backflushing events, temporarily allowing improved sampling of the soot.. 35

Figure 25. Dimensionless extinction coefficient of soot collected from the various flames investigated in this study. Filled symbols denote samples collected from pulsed flames operating at a 15 Hz pulsing frequency. Results from the 635 nm laser source are shown in the upper plot and results from the 1310 nm laser source are shown in the lower plot. 36

Figure 26. Photograph of thermophoretic sampler for collecting representative soot samples onto a TEM grid. Compressed air lines are attached to a pneumatic cylinder at the left of the photo. When activated, the cylinder drives a thin "tongue" containing the TEM grid through the slotted opening at the end of the brass cap (right). The cap acts to deflect sideways (away from the flame) the significant blast of air that is carried with the moving drive rod. 38

Figure 27. Sample TEM image of soot aggregates from the ethylene Wolfhard-Parker flame collected on a lacey grid.....38

Figure 28. Simultaneously excited OH and PAH PLIF images of the steady ethylene Wolfhard-Parker flame with insertion of the thermophoretic sampler tongue into the flame. For this demonstration, the sampler operated with a 40 ms hold time. The tip of the sampler appears as a sharp scattering signal to the flame side of the right-hand PAH layer in each image. Laser light propagates from right-to-left in each image, revealing the shadowing effect of the sampler tongue tip. 39

Figure 29. Photographs showing (a) experimental setup for radiometer measurements in the Wolfhard-Parker burner, and (b) setup for blackbody calibration of radiometer. 40

Figure 30. Radiometry measurements of the radiant emission profiles from steady normal and inverse slot flames. 41

Figure 31. Time record of radiant emission from the 15 Hz pulsed ethylene slot flame at a height of 30 mm and a transverse position of 3 mm from the centerline. 41

List of Tables **Page**

Table 1. Measurement Strategy....14

Table 2. JP-8 Surrogate Mixture (Univ. of Utah "Hex-12")....16

Table 3. Flowrates of Investigated Wolfhard-Parker Flames....18

Table 4. Flowrates of Investigated Coannular Flames....20

Acknowledgments

This project succeeded because of the contributions of a large number of individuals throughout Sandia. Sheldon Tieszen of the Fire Science and Technology group aided in the original formulation of the project plan, in explaining the importance of the project to Sandia managers, and in providing encouragement during the course of the project. Gian Sclippa and Gil Hofacker aided in the design and construction of the slot burner. Al Salmi designed and constructed the coannular burners as well as various mechanical pieces necessary to perform the burner measurements. Doug Scott aided in the implementation of the soot thermophoretic sampler and in the packaging of the radiometry diagnostic. Matt Boisselle and Bob Harmon provided a variety of day-to-day assistance in the laboratory, ranging from Labview data acquisition support and flow controller installation and calibration to laser maintenance and alignment.

Several individuals outside of Sandia also aided in the success of this project. Professor Constantine (Dino) Megaridis of the University of Illinois at Chicago provided critical advice on the design of a low-disturbance thermophoretic soot sampler and also provided soot grid holder "tongues" that are a key part of this design. Pascale Desgroux of the University of Lille, France, graciously agreed to work on this project for several months during its first year and aided in the OH LIF and OH absorption setups and the selection of excitation lines for OH. Pascale also helped determine suitable operating conditions for the methane and ethylene slot flames.

The efforts of all of these individuals, and any we have failed to mention here are appreciated and were essential to the successful completion of this project.

Introduction

This report documents the results of a Laboratory Directed Research and Development (LDRD) project with the aim of compiling a unique, comprehensive database of measurements associated with soot formation, transport, and radiation in a series of steady and pulsed laminar buoyant diffusion flames. A combination of laser-based nonintrusive measurements and extractive measurements of soot microstructure and optical properties was proposed, utilizing the expertise of several investigators at Sandia's Combustion Research Facility (CRF) as well as investigators in the Fire Science and Technology (FS&T) and Thermal/Fluids Experimental Sciences groups.

This project was motivated by the need to develop improved constitutive models for soot formation and radiation in large pool fires. Fires pose the dominant source of risk to the safety and security of nuclear weapons, nuclear transport containers and DOE and DoD facilities. Because of the relatively low velocities (especially near the pool surface), high temperatures, and high soot loadings in pool fires of practical transportation fuels, the predominant mode of heat transfer to significantly sized objects that are engulfed or adjacent to these fires is thermal radiation from soot (Gritzo et al., 1998). The magnitude of this radiant emission is linearly dependent on soot concentration and emissivity and is dependent on soot temperature to the fourth power. It is therefore necessary to understand the local transport and chemical phenomena that determine the distributions of soot concentration, its optical properties, and its temperature, to develop constitutive models required for high-fidelity fire simulations. This information is also critical for the validation of any such models that are developed.

Overview of Soot and Radiation Modeling

Soot formation has been a topic of significant interest to the combustion research field for decades, because soot is a pollutant emission from some combustion systems (such as diesel engines and gas turbines), it hinders safe egress during accidental fires, and thermal radiation from soot is an important contributor to the heat transfer from many combustion systems and from fires. In recognition of the important role of soot in many practical combustion applications, a large number of studies have been performed on soot formation, and occasionally on soot oxidation, in laminar, steady flames burning simple aliphatic hydrocarbon fuels, such as methane, ethylene, and propane. A limited number of studies have included practical transportation fuels such as diesel or kerosene, or have investigated soot formation in steady turbulent or laminar time-varying diffusion flames. Existing experimental databases in moderately and strongly sooting flames have employed a severely limited set of diagnostics, because of the cost of the necessary equipment and the difficulty in applying most diagnostic techniques in sooty environments. Several models describing the evolution of soot particle number density and soot volume fraction have been developed that include the effects of soot particle inception, surface growth, agglomeration, and oxidation (Kennedy, 1997). These reduced chemical models for soot formation have all have shown limited success outside of the steady, laminar diffusion flames in which they were originally calibrated, presumably as a consequence of the limited experimental measurements and thus limited understanding of the key factors influencing soot formation and oxidation rates.

At the level of fundamental physics, the radiant exchange associated with soot is dependent on its overall position within the flowfield, its concentration, its optical properties, and its temperature.

These properties are, to a large extent, determined by the temporal history of the soot formation and oxidation processes. The local soot concentration evolves over time with contributions from convection, molecular transport (principally thermophoresis), local production, and local oxidation. Current soot models focus on the production and oxidation terms and are fit to data employing average temperatures. Transport effects are implicitly included and the exact temperature of soot particles in or near the flame fronts (which largely determines the emission) is not known. Models are therefore only strictly applicable at the conditions for which the data were acquired. It is perhaps for this reason that these models have not generally been successful in making predictions outside of the data acquisition flowfield from which they were generated. For application to large fire simulations, these same soot formation models are used and will likely find similar limitations. To the extent that molecular transport of soot influences its production and oxidation rates, as well as temperature, the contribution of molecular transport needs to be fully understood and measured. The expectation is that thermophoresis has an especially important effect on the magnitude of soot radiation, because of the strong dependence of soot radiation on temperature and because the high-temperature edge of the soot layer is typically located in the region of strongest temperature gradient. Therefore, there is an immediate need to gain a more fundamental understanding of the relevant processes and physics of soot formation in flames, and to obtain the data necessary to develop and validate models for soot formation and radiation that are applicable to large-scale fire simulations.

Measurement Approach

Sandia, with its extensive experimental capabilities and its expertise in fire science and soot diagnostics, is in a unique position to develop the database that is required to generate predictive soot and radiation models applicable to pool fires. The approach developed in this project was to use the pulsed laser capabilities of the CRF's Turbulent Combustion Laboratory (TCL) for a variety of planar imaging diagnostics, in combination with low-power tunable diode laser (TDL) measurements of gas species concentrations, local heat flux measurements, and extractive measurements of soot microstructure and dimensionless extinction coefficient. The list of properties to be measured and the associated diagnostic technique(s) is shown as Table 1.

The measurement properties and the associated diagnostic techniques listed in Table 1 were selected on the basis of the importance of the measured property to an understanding of soot formation, transport, or radiation and on the availability of the appropriate measurement technique at Sandia. Measurements of the hydroxyl radical (OH) are important both as a marker of the high temperature reaction zone and because OH is the predominant oxidizer of soot in flames. Qualitative measurements of total PAH, as provided by their broadband LIF signal, are important in demarking the molecular growth region of flames and also because it is believed that PAH are involved in soot particle nucleation and that they contribute to soot mass growth. Acetylene measurements, provided by tunable diode laser absorption spectroscopy (TDLAS), provide important information on the spatial distribution and the concentration of this important gas species for soot inception and soot mass growth. Acetylene measurements have only rarely been reported in sooty flames, and only when using an extractive probe with analysis by mass spectrometry. The TDLAS technique also is used to measure the water vapor distribution, which is useful for comparing with model predictions of the variation in mixture fraction through the flame. Temperature measurements are obviously important through the soot layer for predicting the soot radiant emission, but full-field temperature measurements are also important for comparing with model calculations of the flame shape and for calculation of the thermophoretic transport of soot. In this project, two-dimensional 2-color pyrometry of the soot layer was

performed, and the recently developed technique of filtered Rayleigh scattering (FRS) was attempted for full-field measurements. The velocity field in these flames is important for understanding of the overall fluid dynamics, including local flame stretch, and also provides the temporal coordinate associated with soot formation and growth. Particle image velocimetry (PIV) is the technique utilized here to measure the instantaneous velocity field. Soot volume fraction, a measure of soot concentration, is important to defining the rate of soot production and destruction and also for interpretation of the soot radiant emission intensity. Laser-induced incandescence (LII) is the pulsed laser technique that is used to provide instantaneous, two-dimensional soot volume fraction. The LII measurements are calibrated by laser extinction measurements. In order to perform this calibration, the dimensionless extinction coefficient (K_e) of the soot in question must be assumed or measured. In this project, we use a transmission cell reciprocal nephelometer (TCRN) to measure K_e. Calculation of the surface-specific soot formation and oxidation rates are dependent on realistic assessments of the soot primary particle size as a function of position in the flames. This quantity, in addition to the overall aggregate structure of the soot particles, is provided by thermophoretic sampling of the soot onto transmission electron microscopy (TEM) grids, with subsequent TEM analysis. These structural measurements may also be combined with the K_e measurements to provide estimates of the absorption coefficient of the soot, as required for predictions of soot radiant emission. Qualitative information on soot radiant emission is provided by flame imaging through a selected bandpass in the near-infrared. Finally, measurements of the local radiant emission, with contributions from both soot and gas radiation, are provided by a thermopile coupled to a long, thin light pipe. More details about these measurement techniques are provided in subsequent report sections.

Table 1. Measurement Strategy

Measurement Property	Diagnostic Technique(s)
OH †	PLIF
C_2H_2, H_2O	TDLAS
PAH	PLIF
T	FRS, soot pyrometry
v	PIV
soot f_v	PLII, extinction
soot microstructure	TEM
soot K_e	TCRN
soot radiation	near-IR emission
local radiant heat flux	thermopile

† OH = hydroxyl radical
C_2H_2 = acetylene
PAH = polycyclic aromatic hydrocarbons
f_v = volume fraction
K_e = dimensionless extinction coefficient
PLIF = planar laser-induced fluorescence
TDLAS = tunable diode laser absorption spectroscopy
FRS = filtered Rayleigh scattering
PLII = planar laser-induced incandescence
TEM = transmission electron microscopy
TCRN = transmission cell reciprocating nephelometer

Burner and Flame Specification

Several of these diagnostic techniques are based on line-of-sight absorption or emission, and therefore greatly benefit from using a long slot flame. These techniques include soot extinction, radiant emission, and tunable diode laser absorption measurements. In addition, the OH PLIF is calibrated by performing OH absorption measurements, which are more accurately performed on a slot burner. For sooty flames, as investigated here, even those diagnostic techniques that do not inherently benefit from a slot geometry in comparison to a coannular geometry *do* benefit from the lack of a curved soot layer between the plane of excitation and the camera detector in a slot flame. Therefore, in this project the most complete set of measurements was performed on a laminar Wolfhard-Parker burner (a slotted diffusion flame burner) that can be operated in either a steady flame mode or an unsteady forced mode. Whereas a coannular geometry is clearly preferred over the slot geometry for flame modeling, it has been previously demonstrated that the slot geometry is reasonably amenable to detailed combustion modeling (Leung and Lindstedt, 1995). However, because of the inherent instability of this type of flame, wire mesh screens must be used at relatively low heights to stabilize the flames, such that soot oxidation and/or radiative quenching of the flame sheet cannot be investigated in this flame system. Because transient soot oxidation and radiative quenching are thought to be important phenomena in aviation fuel pool fires, a coannular, coflow laminar diffusion flame burner was also constructed and interrogated.

For investigation of unsteady vortex-flame interactions in both Wolfhard-Parker and coannular flames, loudspeakers were used on the fuel stream to sinusoidally modulate the fuel flow at low frequencies (on the order of 10-20 Hz), thereby exciting the natural buoyant instability that produces pool fire puffing (and candle flame flicker). By locking the frequency of this instability to that of the loudspeaker excitation, perfectly reproducible flame cycles can be interrogated at specified cycle phases by the different diagnostic techniques.

In addition to the considerations given above for "normal" diffusion flames, wherein an overabundance of oxidizer surrounds a central fuel jet, it was desired to make a subset of measurements in "inverse" diffusion flames, where the relative positions and overall abundances of fuel and oxidizer are reversed. This type of flame geometry is believed to be reasonably common within large fire plumes as turbulent eddies occasionally mix relatively small amounts of air into a large fuel core, but no definitive comparison of soot formation and radiation in these two types of flames has previously been performed (Shaddix et al., 2004-1). Therefore, measurements were made in inverse flames established on the slot burner, where direct, quantitative comparison of radiation intensities could be readily made.

The fuels chosen for investigation in this study were methane, ethylene, and JP-8 surrogate. Methane and ethylene were chosen because of their ease of use, their predominant use in previous studies of sooty flames, and the wide range of soot concentrations produced with these two fuels. An inclusion of JP-8, the target fuel for most of Sandia's interest in large pool fires, was felt to be important, but for the sake of ease of future modeling and for future experimental reproducibility a surrogate mixture for JP-8 was used. Because of the need to keep all of the fuel tube heated above the top end of the JP-8 distillate curve and the difficulty in modulating the fuel vapor flow, the JP-8 flames were only established on a specially designed coannular burner. More details concerning burner design and the canonical flames investigated are given in the following section.

A number of investigators have recently developed specific mixtures of pure hydrocarbon to act as surrogates for kerosene or specifically for JP-8 (Lindstedt and Maurice, 2000; Edwards and Maurice, 2001; Violi et al., 2002; Agosta et al., 2004). Because of Sandia's close affiliation with the University of Utah in their ASCI-Alliance program, "C-SAFE," and because of the specific focus at Utah on JP-8 surrogates appropriate for modeling large pool fires, we chose to use one of the six component mixtures recommended by the University of Utah (Eddings et al., 2004). This mixture is shown below in Table 2, both in terms of molar composition and liquid volume composition. This mixture has a molecular weight of 152 g/mol, a liquid density of 0.818 g/ml, and a stoichiometric molar air/fuel ratio of 100.6. The surrogate mixture was produced at Sandia in 500 ml increments with an accuracy of greater than 1 ml volume addition of each component. The components were obtained from Fischer Scientific and Sigma-Aldrich and had purities of ≥ 98%. Initial liquid fuel flame tests were performed with common household kerosene, obtained from the local Orchard Supply Hardware store. The observed flame properties (height and luminosity) were nominally the same between the surrogate mixture and the hardware store kerosene.

Table 2. JP-8 Surrogate Mixture (Univ. of Utah "Hex-12")

Component	Chemical Class	Molecular Formula	Mole-%	Volume-%
isooctane	branched alkane	C_8H_{18}	3	3
xylenes	aromatic	C_8H_{10}	15	10
tetralin	cycloalkane/aromatic	$C_{10}H_{12}$	13	9
decalin	cycloalkane	$C_{10}H_{18}$	27	22
dodecane	normal alkane	$C_{12}H_{26}$	30	37
hexadecane	normal alkane	$C_{16}H_{34}$	12	19

Burners and Flames

Wolfhard-Parker Burner

A large Wolfhard-Parker burner was used to support laminar diffusion flames of methane/air and ethylene/air (see Figs. 1 and 2). The overall dimensions of this burner are similar to one previously investigated at Sandia by Schefer and coworkers (Najm et al., 1998; Mueller and Schefer, 1998). The central, rectangular slot is 12 mm wide by 95 mm long. Coflow is introduced on each of the long sides of the slot and nitrogen gas is introduced at the short ends of the slot to prevent the formation of end-flames. The flame sheets are confined and protected from room air disturbances by a rectangular chimney enclosure with a cross-section of 140 mm x 191 mm. Within the chimney, two curved wire mesh screens form a two-dimensional contraction to assist in stabilizing the flame. UV-quality quartz windows provide optical access from all four walls of the enclosure. For studies of pulsed flame behavior, the central flow is modulated by two 100-mm diameter loudspeakers that face each other across the slot, well below the burner face. Power spectral density analysis of the flame emission from the unstable regions of the nominally "steady" flames (well above the height at which measurements are normally made) revealed that the natural puffing frequency of the burner is 11 Hz.

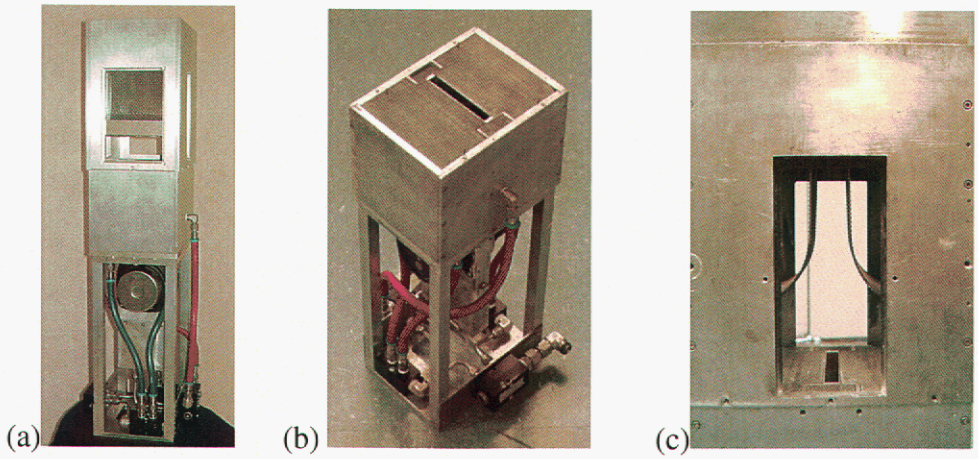

Figure 1. Photographs of Wolfhard-Parker burner (a) from the side of the slot, showing loudspeaker and chimney enclosure with optical access window and stabilizing screen, (b) looking down at the burner face with the chimney removed, and (c) looking down the axis of the slot with "gull wing" stabilization screens in view.

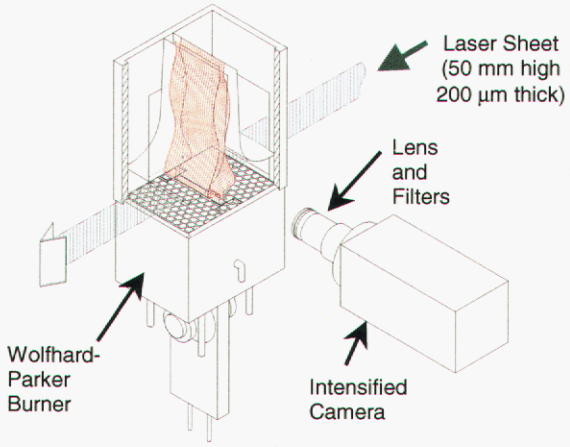

Figure 2. Schematic of Wolfhard-Parker burner with laser sheet and intensified CCD camera for flame imaging.

Air, fuel, and nitrogen flows to the burner were metered using calibrated mass flow controllers. For the experiments involving normal diffusion flames (NDFs), fuel was fed to the slot and air formed the coflow. To form inverse diffusion flames (IDFs), these connections were reversed. Fuel and air flow parameters for the investigated flames are shown in Table 3. The NDFs extended nearly 0.50 m above the top of the chimney, for a total flame height of approximately 0.70 m. Calculations using the Roper correlations for flame heights of laminar jet diffusion flames (Roper, 1977) suggest that essentially the same flowrate of air will yield a common flame height for methane and ethylene IDFs. Therefore, a common air flowrate of 30 slpm was used for these two IDFs, and indeed these flames both had a height of 80 mm, as determined from the location of the dark inner edge of the luminous zone. This choice of air flow yielded relatively stable IDFs with near-vertical flame sheets in the 50-mm high interrogation region at the base of the flames, similar to the NDFs. The methane and ethylene fuel flows in the IDFs were set to the

50 slpm maximum flow capability of the fuel flow handling system, to improve flame stability and minimize product recirculation.

Table 3. Flowrates of Investigated Wolfhard-Parker Flames

Flame	Q_{fuel} (slpm)	Q_{air} (slpm)	V_{fuel} (cm/s)	V_{air} (cm/s)	slot Re	ϕ [a]
CH_4 NDF	15.0	250	22.3	17.6	270	0.57
C_2H_4 NDF	7.5	250	11.2	17.6	260	0.43
CH_4 IDF	50	30.0	3.5	44.6	590	15.8
C_2H_4 IDF	50	30.0	3.5	44.6	590	23.7

[a] global stoichiometry of gases supplied to the burner

For operation of the methane IDF, an outlet screen was necessary to prevent self-ignition of the fuel-rich product gases. Recirculation of soot and tar-laden gases occurred along the sides of the chimney enclosure when operating IDFs of either fuel, resulting in attenuation of the incident laser beam and of the imaged optical signals. To address these difficulties, a chimney extension was incorporated, which confined the product gas recirculation to a region above the stabilizing screens (see Fig. 3).

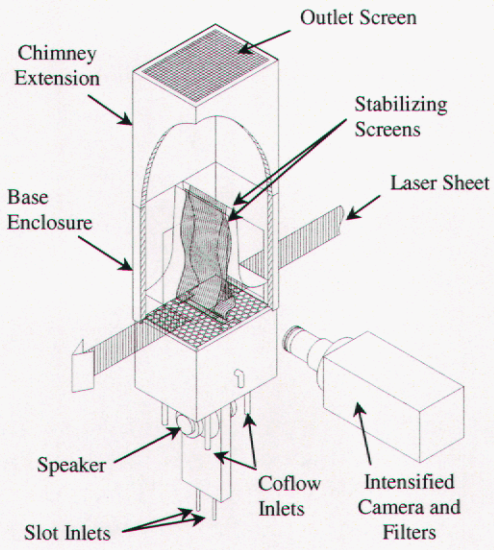

Figure 3. Schematic of Wolfhard-Parker burner with chimney extension and outlet screen for operation of inverse diffusion flames.

Figs. 4–5 show photographs of the steady and pulsed Wolfhard-Parker diffusion flames. With the use of the slot flame geometry, the blue CH* chemiluminescence, marking the fuel-rich edge of

the reaction zone (Schefer, 1997), is clearly seen to lie outside of the yellow-orange soot luminosity for the NDF and inside of the luminous zone for the IDF (Fig. 5). Fig. 4 demonstrates the uniform flame behavior along the slot that was achieved for the normal diffusion flames.

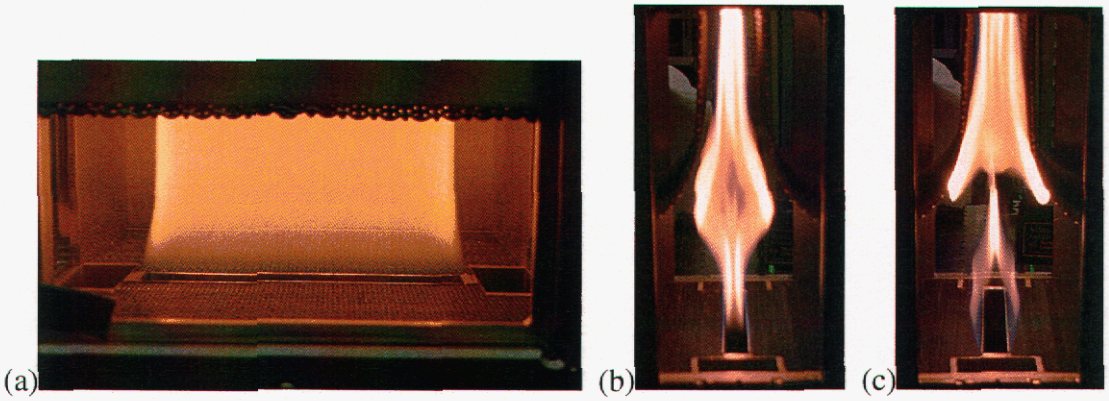

Figure 4. Photographs of ethylene/air Wolfhard-Parker normal diffusion flames: (a) side-view of steady flame, with the bottom edge of the stabilization screen evident, (b, c) two different phases of the pulsed flame.

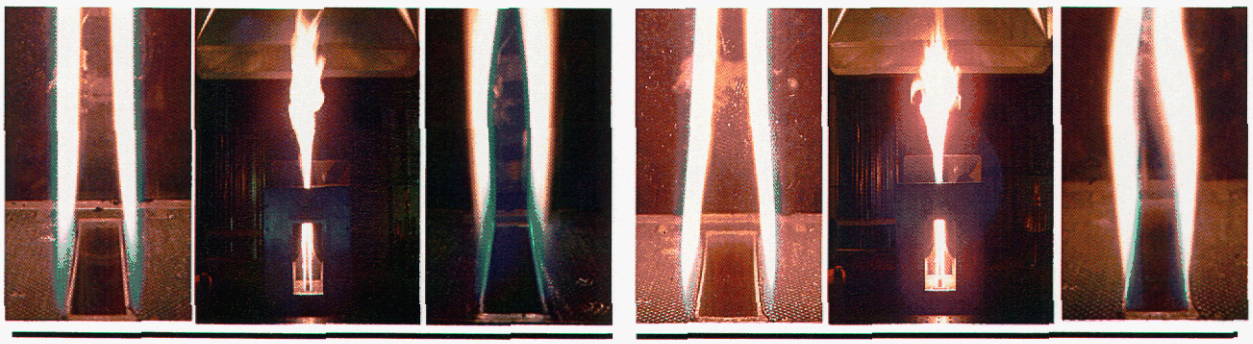

Figure 5. Photographs of investigated steady Wolfhard-Parker flames, showing (from left to right, for each fuel) a close-up of the NDF, a distant view of the NDF, and a close-up of the IDF.

Gas Fuel Coannular Burner

After reviewing the literature of soot formation studies in laminar, coannular diffusion flames and considering the tradeoffs of spatial resolution of intensified CCD (ICCD) imaging and maximum imaging height per image, it was decided that the best choice of burner tube diameter would be the ½-inch tube used by Mitchell and coworkers (Mitchell et al., 1980), Santoro, Dobbins and coworkers (Santoro et al., 1983, 1987; Santoro and Semerjian, 1984; Megaridis and Dobbins, 1989; Puri et al., 1992, 1993, 1994; Dobbins et al., 1995, 1998), Smyth and coworkers (Smyth et al., 1993; Shaddix et al., 1994; Shaddix and Smyth, 1996; Smyth et al., 1997), and McEnally, Pfefferle and coworkers (McEnally and Pfefferle, 1996, 1998a, 1998b; Smooke et al., 1999). In contrast to previous studies, however, we designed a square burner face and chimney enclosure, facilitating laser sheet imaging measurements of the flame (see Fig. 6).

The fuel and air flowrates chosen for the coannular flames are shown in Table 4 and photographs of the steady flames are shown in Fig. 7. Fuel flowrates were chosen to yield similar visible flame heights for the steady flames and sufficiently short, pulsed flames that could be fully interrogated through the burner chimney windows. In addition, the choice of fuel flow in the ethylene flame was made to yield the same steady flame height as that of the "non-smoking" or "NS" flame extensively investigated by Santoro, Dobbins, and coworkers (Santoro et al., 1983, 1987; Santoro and Semerjian, 1984; Puri et al., 1992, 1993; Dobbins et al., 1995, 1998). The coflow of air was chosen to yield optimal stability in the steady flames. This value is significantly higher than that generally used for the "NS" flame (43 slpm).

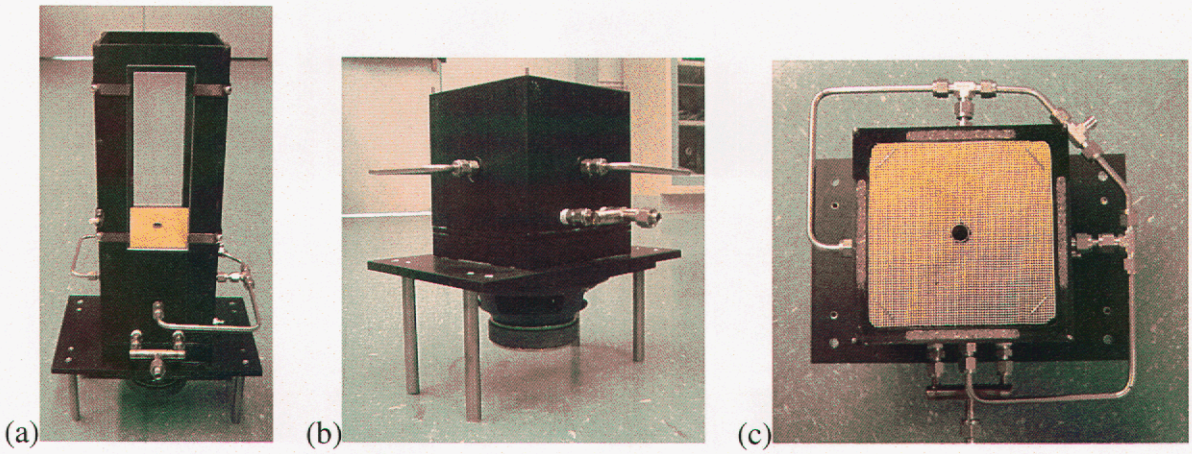

Figure 6. Photographs of coannular gas fuel burner (a) with chimney attached, showing optical access windows, (b) side profile, showing loudspeaker on burner base, and (c) looking down on the burner face, with ceramic honeycomb and central fuel tube.

Table 4. Flowrates of Investigated Coannular Flames

Flame	Q_{fuel} (slpm)	Q_{air} (slpm)	V_{fuel} (cm/s)	V_{air} (cm/s)	tube Re	ϕ [a]	h_f (mm) [b]
CH_4	0.44	350	8.2	35.3	274	0.012	84
C_2H_4	0.22	350	4.1	35.3	258	0.009	88
JP-8 surrog. + N_2 diluent	0.0335 0.107	350	2.6	35.3	41 [c]	0.010	40 [d]

[a] global stoichiometry of gases supplied to the burner
[b] visible flame height
[c] at 327 °C
[d] height of strongly luminous zone (smoking flame without a well-defined flame height)

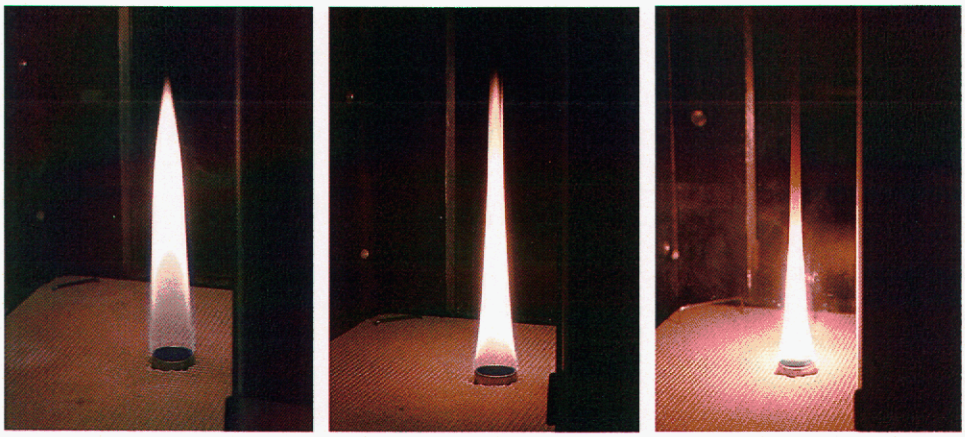

Figure 7. Photographs of steady methane, ethylene, and JP-8 surrogate coannular flames.

Liquid Fuel Coannular Burner

There have been few studies of liquid-fueled laminar jet diffusion flames. The vaporizer and burner assemblies that have previously been designed have generally used a diluent carrier gas (usually nitrogen) to sweep the fuel vapor out of a heated vaporization unit before pyrolytic reactions begin to occur in the hot fuel vapor. Those systems employing aromatic fuels have required special sealing materials in heated vapor delivery lines, with the vaporizer and delivery system placed in a fume hood. The difficulty of handling hot fuel vapor increases with the temperature required to vaporize the fuel. In our case, the top end of the kerosene distillation curve is approximately 300 °C (Eddings et al., 2004), posing daunting requirements for sealing of a heated fuel delivery line. To circumvent these difficulties and eliminate the need for a fuel line ventilation system, we decided to use a novel ceramic, capillary force vaporization system and attach it to the bottom of the fuel tube in the coannular burner (Fig. 8). The vaporizer is manufactured by Vapore, Inc., based in Richmond, California, that specializes in vaporization of practical hydrocarbon fuels. The vaporizer base unit itself is not designed to operate correctly at elevated temperatures, so we implemented an insulating seal between the heated fuel tube and the base unit and attached a heat dissipation fin section, with attached fan, to the bottom of the base unit (Fig. 8). The fuel tube is heated by a coil heater to 350–380 °C, well above the upper limit of the distillation curve, to maintain the evaporated fuel in the gas state.

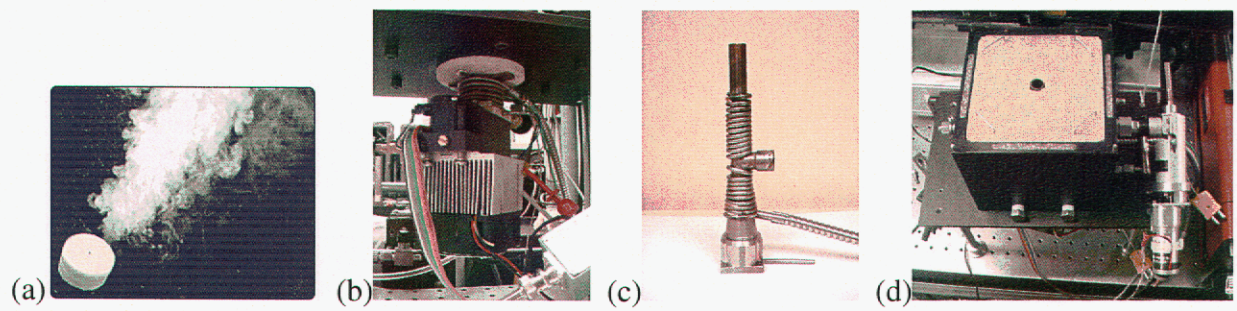

Figure 8. Photographs of (a) capillary force vaporizer, with fuel vapor jetting from central hole, (b) vaporizer unit attached to bottom of burner, with cooling fins and fan, (c) fuel tube, with coiled heater and sidearm connection, and (d) assembled burner, with model airplane piston attached to modulate fuel flow.

To modulate the fuel flowrate and yield reproducible, pulsed flames, a model airplane piston, driven by an electric motor, is attached to a sidearm that connects into the vertical fuel tube. For simplicity in design and operation, the sidearm was not heated. Unfortunately, with this design some of the vaporized fuel condensed within the sidearm, resulting in unsteady flame operation. We found that by providing a small flow of nitrogen diluent at the base of the fuel tube, this problem could be avoided and the flame would have good stability and reproducibility. Consequently, the measurements of the JP-8 surrogate flames were performed with a diluted flow of fuel vapor. This had the additional advantage of reducing the local soot concentrations in the flames to levels that were more manageable for the different diagnostic techniques.

Choice of Unsteady Flame Conditions

Once steady flame flowrates had been chosen, the appropriate conditions to investigate for unsteady flames needed to be determined. The intent in this project was to modulate the fuel flow rate at a frequency in the vicinity of the natural buoyant instability frequency of the flames, thus triggering repeatable generation of air-side vortical structures that would induce compressive and extensional strain on the flame as the vortices propagated vertically up the sides of the flame. For the Wolfhard-Parker burner and coannular burners used in this study, the natural resonant frequency of the buoyant instability is about 10 Hz, as predicted by experimental correlations (Hamins et al., 1992; Cetegen and Ahmen, 1993; Thuillard, 2002) and determined explicitly in this study. But decisions were required for the precise pulse frequency, or frequencies, that should be used for the canonical unsteady flames to be interrogated, and what extent of fuel forcing should be used?

With respect to forcing frequencies, one consideration was the ease with which phase-locked measurements could be achieved with the different laser diagnostic techniques. The Nd:YAG-pumped dye laser system that was used for OH and PAH PLIF measurements can be operated at pulse repetition rates ranging from 7.5 to 10 Hz. The PIV laser system is designed to operate at a 15 Hz pulse repetition rate, but can have its Q-switch triggered to as low as 7.5 Hz. Therefore, we determined it was simplest to achieve phase-locking for frequencies spanning approximately 5-30 Hz by pulsing the flames at multiples of 7.5 Hz.

In considering the appropriate pulse amplitude to apply, knowledge of the actual extent of flow modulation was not known *a priori* – only the voltage applied to the loudspeaker(s) and the observed flame behavior were known until a detailed set of PIV data could be collected later. Consequently, the fuel modulation amplitude for the candidate flames was chosen to be the smallest value such that, for the modulation frequencies investigated, substantial flame movement was evident. In this way, the choice of fuel modulation amplitude was coupled to the choice of modulation frequencies. To simplify the choice of fuel modulation amplitude, it was decided to use the same loudspeaker forcing amplitude for both methane and ethylene slot flames, although the higher fuel flowrate of methane flames meant that a given loudspeaker forcing amplitude resulted in a lower relative flow modulation. In fact, the observed flame response for the methane and ethylene slot flames was similar for a common loudspeaker forcing amplitude. For the coannular flames, the methane flame was excited much more easily than the ethylene flame, so that a significantly lower forcing voltage was used for methane. For the liquid-fueled coannular burner, different piston assemblies were tried until the correct degree of flame oscillation was observed for a piston with a 11.7 mm bore and 5.6 mm stroke (0.60 cc displacement). We used a common loudspeaker voltage when investigating the behavior of

different forcing frequencies, although the loudspeakers potentially produce a different displacement depending on the forcing frequency.

With the above considerations in mind, the methane and ethylene slot flames were investigated using simultaneous OH and PAH PLIF (described in the next section) phase-locked to the sinusoidal oscillation of the loudspeakers. Full sets of images were collected for forcing frequencies of 7.5 Hz, 15 Hz, and 22.5 Hz. As the forcing frequency was extended to higher or lower frequencies than these, the magnitude of flame perturbation decreased. In addition, the flame response became chaotic for frequencies around 30 Hz. After settling on the use of a forcing amplitude of 5.0 volts applied to the two 4-inch loudspeakers on the fuel slot, it was noted that the 15 Hz and 22.5 Hz methane flames and the 22.5 Hz ethylene flame could be locked at one of two different cycle evolutions, depending on the vagaries of when the triggering was initiated. Further investigation verified that in fact this behavior resulted from the flames oscillating at a characteristic frequency of f/2, where f was the forcing frequency applied to the fuel flow. This behavior, previously unreported, was thoroughly investigated in this study by using a laser beam deflection diagnostic aligned in the direction of the fuel slot (see Fig. 9). Power spectral density analysis of the time records of laser beam transmission clearly revealed the important frequency components of the flame and allowed "stability maps" to be generated for the methane and ethylene flames, showing where the flames characteristically responded to the forcing at a frequency equal to f, f/2, f/3, or even a lower subharmonic of the forcing frequency (Williams et al., 2003; see Fig. 10). In all cases, the subharmonic response of the flame could be rationalized as a means of the flame oscillating at a frequency close to its natural buoyant instability frequency of ~11 Hz.

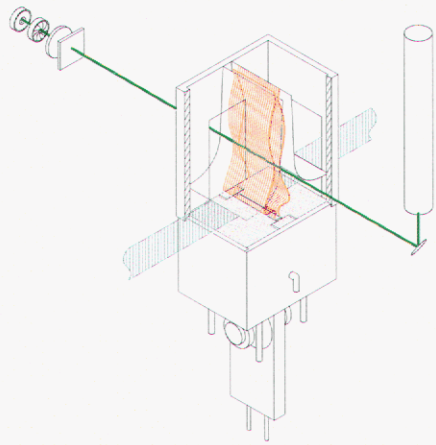

Figure 9. Schematic of pulsed slot burner and associated laser beam deflection and laser sheet imaging diagnostics.

The subharmonic frequency response of these flames turns out to be relevant to the current study both because it provides new information regarding the nature of the fundamental buoyant instability of fire plumes, which is poorly understood, and because in our forced flames, the subharmonic response can lead to transient flow separation between interior flow regions, where the soot exists, and the high temperature flame zone. To define canonical pulsed flame conditions for construction of our database, we decided to apply all of the diagnostics in 15 Hz pulsed flames and, when convenient, to also collect some data in 7.5 Hz and 22.5 Hz flames.

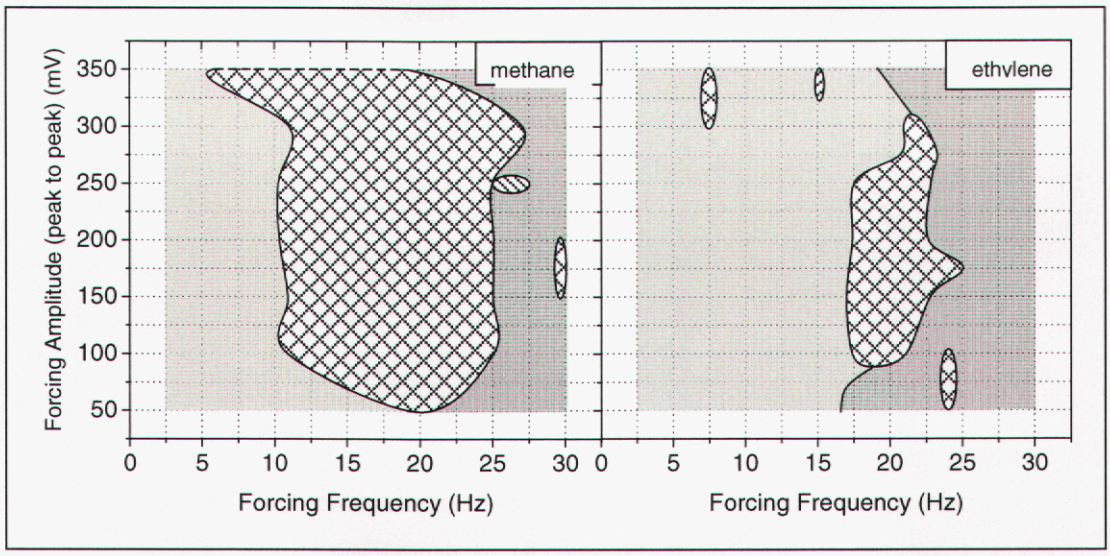

Figure 10. Maps of flame response to fuel forcing frequency and amplitude for the methane and ethylene slot flames:

- broadband stimulation and forcing freq. (f) peak
- f/2 and f peaks plus their higher harmonics
- f peak and higher harmonics
- f/4, f/2 and f peaks plus their higher harmonics
- f/3, 2f/3 and f peaks plus their higher harmonics

OH and PAH, Soot Radiation

A frequency-doubled, Nd:YAG-pumped dye laser provided pulsed ultraviolet light for the simultaneous planar excitation of OH· and PAH fluorescence, as detailed in Smyth et al., 1997. The laser light also excited laser-induced incandescence (LII) emission from the soot particles. The laser sheet was 50 mm high, with a thickness of 250 μm through the flame zone. The beam was used to pump the relatively temperature-insensitive $Q_{21}(8)$ line of the (1,0) band of the OH· $A^2\Sigma^+$–$X^2\Pi_i$ electronic transition at 283.57 nm. The fluorescence and LII signals were collected through a 45-mm focal length, f/1.8 UV lens attached to a gated, intensified charge-coupled device (ICCD) camera. A Schott WG295 long-pass filter eliminated laser reflections as well as scattering from soot particles. For the fluorescence measurements, an additional filter was used to reduce the signal contribution from soot LII, C_2 Swan band emission, and natural flame emission. A 450 nm UV-quality short-pass filter was used for methane flames, whereas a 340 nm band-pass filter was used for ethylene flames. OH and PAH signals were clearly distinguished by tuning the laser off of the OH absorption line. To prevent irising effects with the slow-gating ICCD camera, an intensifier gate width of 200 ns was used for both the fluorescence and LII measurements.

For investigation of the pulsed flames, the speakers were synchronized to the Q-switch sync of the Nd:YAG laser, thus allowing flame excitation frequencies at multiples of the 7.5 Hz flash-lamp frequency. The LIF images were corrected for the mean laser sheet intensity profile determined from 200-shot images of Rayleigh scattering from room temperature air. Shot-to-shot variations in laser power at any given position in the laser sheet were found to average less than

5%. The laser intensities used for imaging were verified to be sufficiently low to produce a linear power dependence for both the OH and PAH LIF.

In addition to these laser-based measurements, natural flame emission at a wavelength of 850 nm was measured through a 10 nm FWHM interference filter. The 850 nm bandwidth filter was chosen for the measurement of the natural radiation because it was the longest wavelength that could be detected with sufficient sensitivity to permit a detection gate width short enough for good phase locking. A longer wavelength is preferred to shorter ones both to avoid contributions from chemiluminescent emissions and to more faithfully track changes in soot radiant emission (which peaks at around 1400 nm in these flames). For the pulsed flame measurements, the natural radiation is phase-locked in the same manner as the laser-based measurements, but uses a 4 μs detection gate width. This corresponds to a phase resolution of a fraction of a degree.

Figure 11 shows simultaneous OH and PAH PLIF images of selected methane, ethylene, and JP-8 surrogate flames. This diagnostic technique reveals the location of the high-temperature flamesheet (via OH LIF), shows the region of fuel-rich molecular growth (via PAH PLIF), and, in strongly sooting flames, also shows the location of the soot layer. Consequently, it is a very useful technique for surveying the dynamic behavior of pulsed flames.

Figure 12 shows images of the 850 nm radiation emission from the 15 Hz pulsed ethylene slot flame. This measurement gives a semi-quantitative assessment of the intensity of thermal radiation from soot in these flames. When these images are viewed alongside the OH and PAH PLIF images (with some soot LII evident), the effect of flame dynamics on the heating of the soot layer is readily apparent. Anywhere the vortex-flame interaction results in straining of the flame, the existing soot layer is driven closer to the high-temperature flamesheet (shown by OH) and gives off much stronger thermal radiation.

Soot Volume Fraction

Soot volume fraction was measured in the canonical flames using the technique of laser-induced incandescence (Santoro and Shaddix, 2002). This technique uses a pulsed laser (in the form of a beam or a sheet) to heat soot particles up to their vaporization temperature (around 4000 K) and then measures the magnitude of the broadband thermal emission from the soot. To avoid interfering signals from PAH LIF and from laser-excited C_2 Swan Band emission, this technique is best performed using a long wavelength excitation laser. In this project, we utilized the fundamental frequency output (1064 nm) from a Nd:YAG laser and expanded it into a two-dimensional sheet. Even after overexpanding and clipping the edges of the sheet, scans of an iris in front of a joule-meter showed a 50% drop in laser fluence near the edges of the 50-mm wide image plane. The LII signal from a given location of the flame varied considerably as the flame was moved both horizontally and vertically across the image plane. The vertical variations result from a combination of CCD intensifier gate irising effects, laser fluence variations, and the LII power dependence curve, whereas the horizontal variations result from a combination of irising effects, laser sheet thickness variations, and the power dependence curve. To minimize the irising effects, while limiting sensitivity to variations in soot primary particle size and laser fluence, a 400 ns intensifier gate width was used on the ICCD, with the gate opening beginning 100 ns before arrival of the laser pulse. Also, the 50-mm images were collected with a 25 mm overlay, such that only the central 25 mm of the images needs to be quantitatively analyzed.

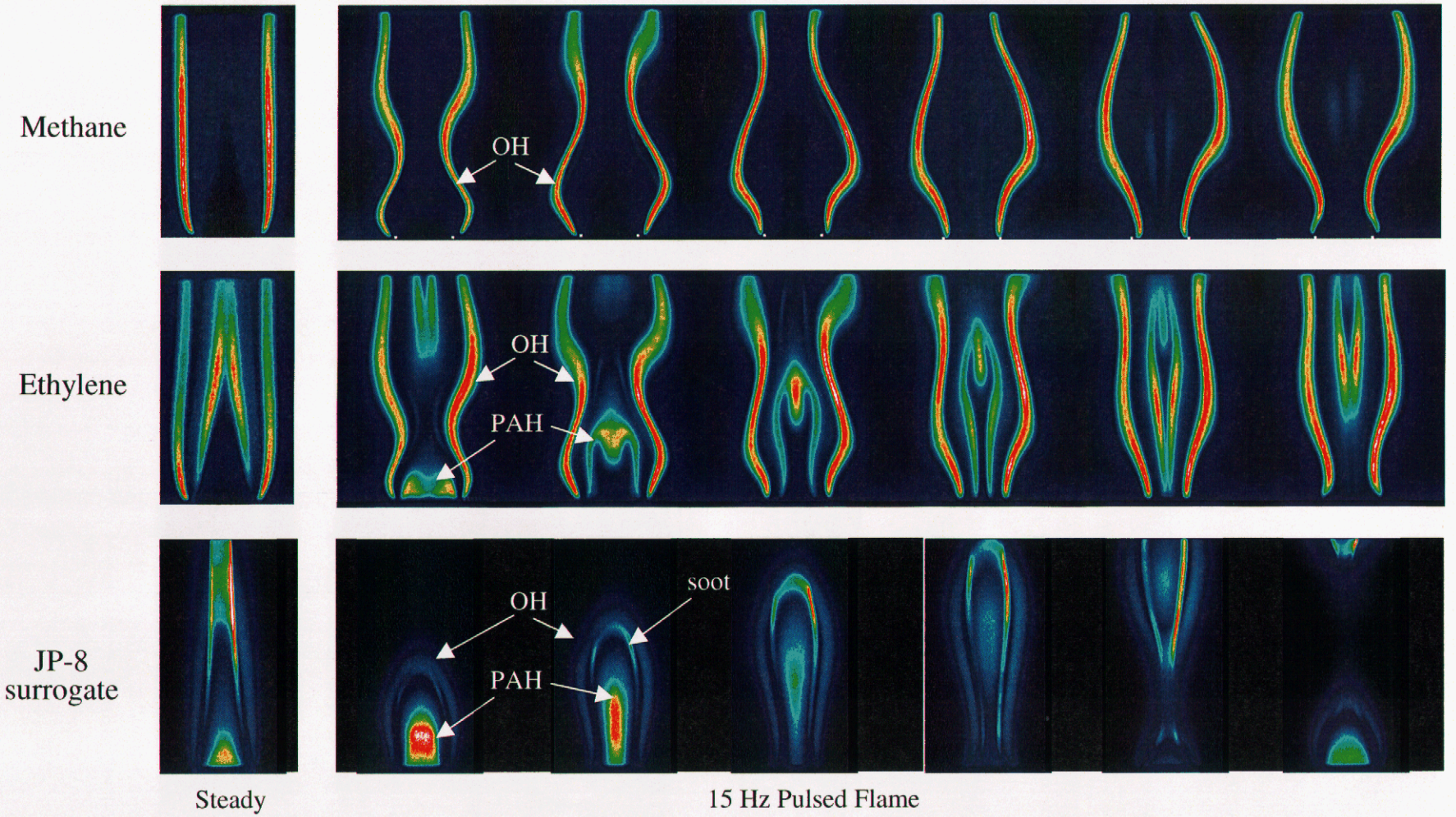

Figure 11. ICCD images (50-mm high) of simultaneously excited OH PLIF and PAH PLIF. The top two rows show images of the steady and 15 Hz pulsed methane and ethylene slot flames. The last row shows images of the steady and 15 Hz pulsed JP-8 surrogate/N_2 coannular flames. Soot LII signals are weakly evident as thin streaks in the pulsed ethylene flames and are strong signals in upper regions of the JP-8 flame.

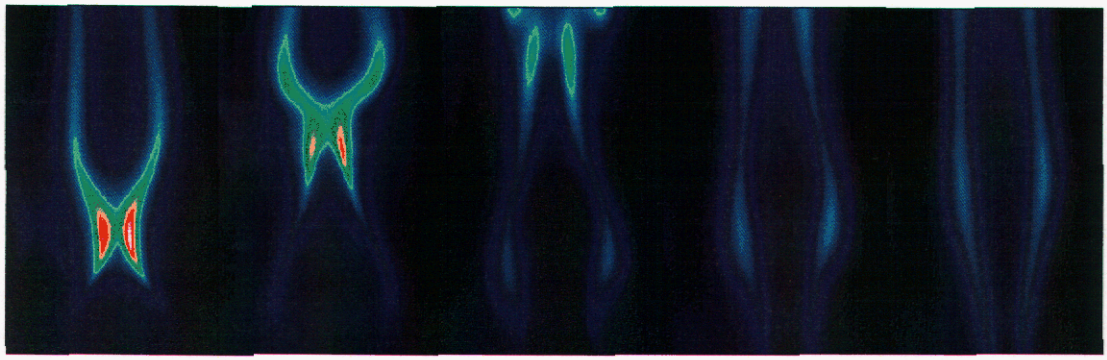

Figure 12. ICCD images (50-mm high) of 850 nm (thermal) emission from the 15 Hz pulsed ethylene slot flame. The phases shown here correspond to the first 5 phases shown for PLIF imaging of this flame in Fig. 11.

Finally, the horizontal and vertical variations in signal response were mapped out in detail, to allow subsequent corrections to be applied, if need be. The LII signals were collected with a 450 nm short-pass filter. An example of LII images is shown in Fig. 13.

Calibration of LII was performed via laser extinction measurements. UV extinction measurements were performed in both methane and ethylene slot flames. In addition, extinction measurements at 1310 and 1540 nm were performed as part of the data collection for tunable diode laser measurements of water vapor and acetylene (described later). Quantification of the extinction measurement in terms of soot volume fraction requires the use of an appropriate dimensionless extinction coefficient, as measured in this project at 635 nm and 1310 nm (described later). The 1310 nm values were used to calibrate the extinction data collected in the slot flames at the same wavelength.

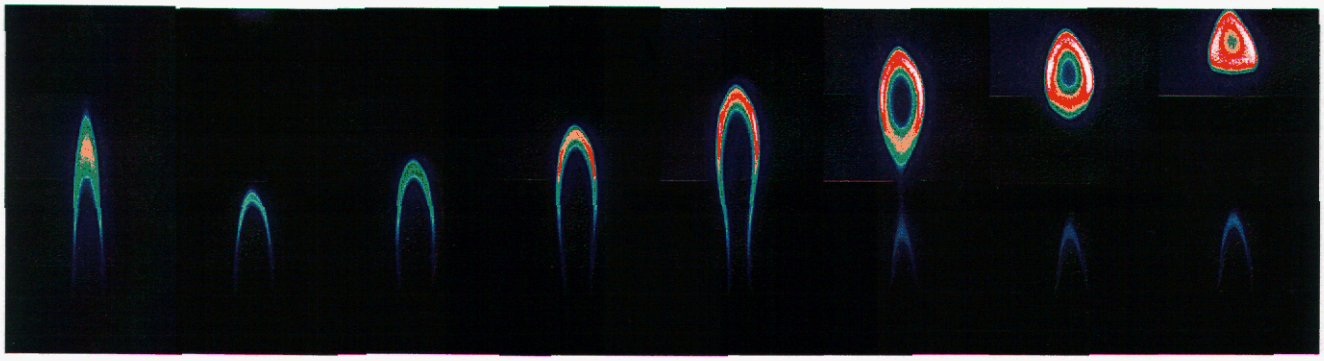

Figure 13. Stacked, planar images of LII from the steady and 15 Hz pulsed methane coannular flame.

Velocity Field

The velocity field was measured using particle image velocimetry (PIV), using a special PIV laser that supplies pairs of second harmonic Nd:YAG pulses at 532 nm with an adjustable time delay between the pulses. The PIV technique relies on tracking the motion of individual seed

particles from the first pulse to the second pulse. High densities of seed particles must be injected into the fuel and air to obtain good velocity maps, especially in the vicinity of the high temperature flame sheet, where gas expansion effects reduce the seed density. The seed particles used in the flames were ceramic microspheres with 10 wt% less than 1 μm, 50 wt% less than 5 μm, and 90 wt% less than 14 μm. Olive oil droplets were used as the particle seed for cold-flow PIV of the velocity fields exiting the fuel and air passages. Fig. 14 shows an example of the transient cold-flow velocity field for pulsed fuel conditions and Fig. 15 shows the air-side buoyant vortex structure that drives the flame pulsing behavior in the unsteady flames.

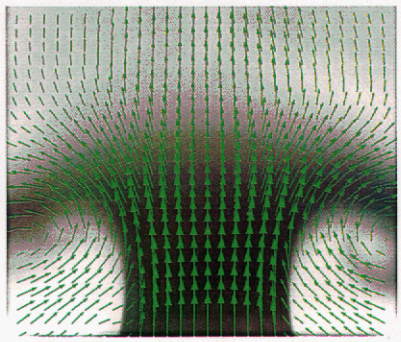

Figure 14. Overlay of ICCD image of (a) light scattering from heavily seeded airflow and (b) velocity vectors, obtained by performing PIV on lightly seeded fuel and air flows. The flow exiting the fuel slot appears dark.

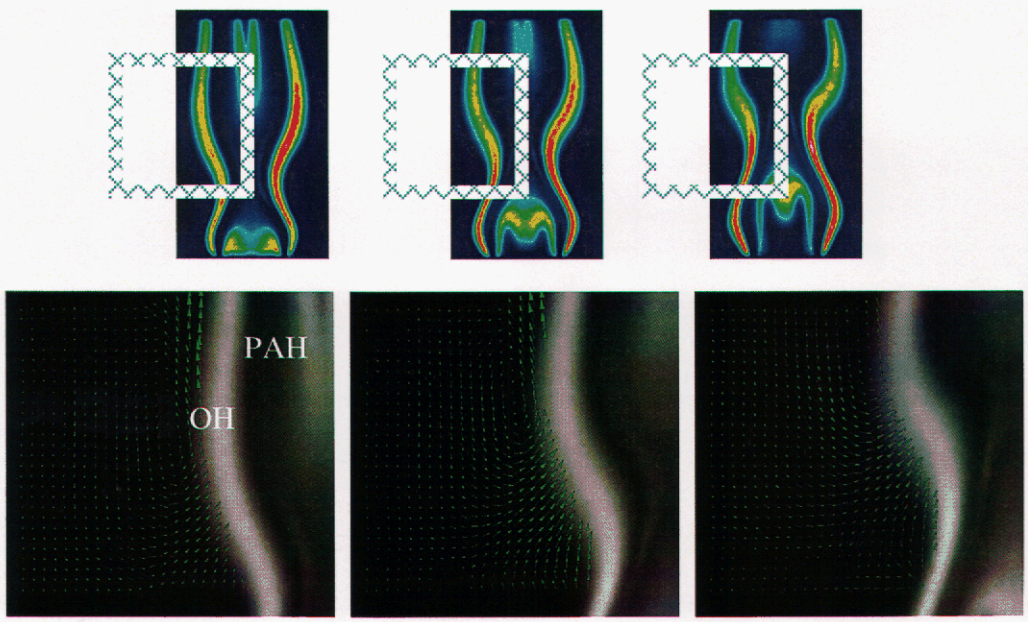

Figure 15. Lower images: overlay of OH/PAH PLIF image and air-side velocity field from the 15 Hz ethylene slot flame for three successive phase increments of 20°. The mean vertical velocity on the air-side of the flame sheet has been subtracted from each of the images to clearly show the embedded vortex structure. Upper images: false color PLIF images, with the regions interrogated in the lower images indicated by squares.

Temperature

Temperature measurements were attempted in two different ways during this project. First, measurements were made in soot-containing regions using calibrated two-color imaging pyrometry. This was accomplished by splitting the naturally emitted light with a large beamsplitter and using two ICCD cameras, at right angles to one another, to image the soot layer at specific wavelengths that are free from significant gas-band radiation. A photograph of the optical arrangement is shown as Fig. 16. Because this technique relies on line-of-sight emission, it is well-adapted to implementation in the Wolfhard-Parker burner flames and can directly utilize existing equations for two-color pyrometry (Murphy and Shaddix, 2004). For application to the coannular flames, the raw data need to be inverted along a given radial line by performing one-dimensional tomography (Dasch, 1992; Snelling et al., 2002). Calibration of the two-color measurement was performed by moving the optical breadboard containing the beamsplitter and ICCDs to a position in front of a high-temperature blackbody source (Micron M330) and focusing the ICCD lenses onto the back wall of the blackbody cavity.

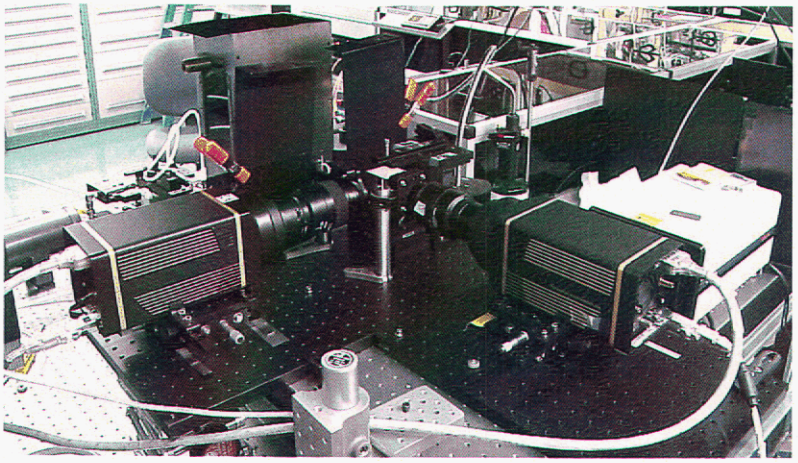

Figure 16. Photograph of 2-color pyrometry imaging setup.

The second technique attempted for temperature measurements was filtered Rayleigh scattering (FRS), which has been recently developed as a promising technique for flowfield imaging measurements of temperature or velocity (in high-speed, isothermal flows) (see Kearney et al., 2004). Implementation of this diagnostic technique requires an injection-seeded YAG laser. For this project, we had the option of sending our burners to Albuquerque, where an FRS diagnostic system is operational, or attempting to construct our own system in the Turbulent Combustion Laboratory utilizing leftover components from a previous FRS setup. A recent study had demonstrated that the high altitude of Albuquerque results in noticeable broadening of buoyant flames (Kearney et al., 2004), so we decided to attempt the FRS measurements in California. A photograph of the optical layout is shown as Fig. 17. The YAG laser we obtained for this purpose had not been using its seeder for quite some time and it took a week's worth of dedicated effort to get the laser operating well. Even then, the first attempts at FRS images showed very weak signals compared to past experience with FRS, so further work on obtaining FRS data was abandoned until other critical measurements were completed. These other measurements consumed the available time until the end of the project, so FRS data was never collected. Based on previous experience of performing FRS in soot-containing flames, it is not believed that this technique will work in most of the flames investigated in this project, because the technique fails

for soot levels on the order of 1 ppm volume fraction (Hoffman et al., 1996; Will, 2001; Kearney et al., 2004). However, it is hoped that FRS measurements can still be attempted on the flames studied in this project as part of a suitable, current project.

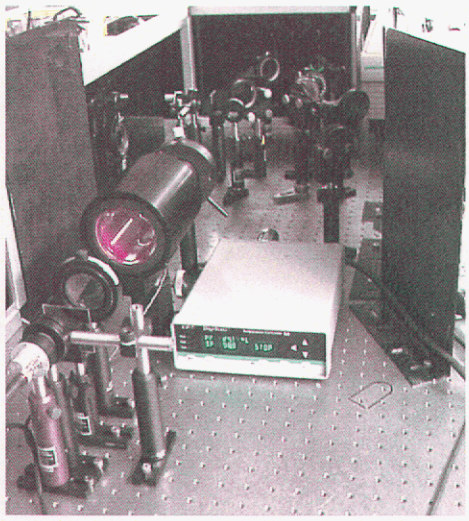

Figure 17. Photograph of filtered Rayleigh scattering diagnostic setup for wavelength scanning and locking of an injection-seeded YAG. The horizontal cylinder on the left is an iodine cell.

Acetylene and Water Vapor

Acetylene and water vapor were measured using tunable diode laser absorption spectroscopy (TDLAS). This is inherently a line-of-sight technique and therefore is well-suited to interrogation of slot flames. In fact, at the near-infrared wavelengths at which the measurements here were performed, the absorption signals were so weak that measurements in the coannular flames were impossible. For the slot flames, suitably strong signals were obtained by passing the beam along the slot axis when applying high-frequency wavelength modulation spectroscopy (wms) to record the signals. To eliminate uncertainties in the phase matching for the lock-in amplifier measurement of the second harmonic signals, the lock-in output was recorded in quadrature, using two separate, custom-designed short time constant lock-in amplifiers (Shaddix et al., 2001; see Fig. 18). Potential water lines to measure were investigated by scanning a nominally 1305 nm TDL whose output was coupled to a Herriott cell in the open air of the laboratory (total pathlength of 4.5 m) and also by testing candidate absorption lines in the slot flames. In the end, an absorption line at 1304.3 nm (in air at STP) was chosen for measurement, based on its signal strength. Acetylene absorption lines that were accessible with a nominally 1548 nm TDL were identified by interrogating a sealed Herriott cell with a 10 m optical pathlength that was filled with 200 ppm of acetylene at 400 torr. Figure 19 shows the acetylene transitions and associated water transitions accessible with the acetylene TDL, based on data in the HiTran compilation (Rothman et al., 1998). Candidate acetylene lines were evaluated for cold or hot water line interferences using the open-air Herriott cell (with ambient moisture) and through evaluation of transverse profiles in the slot flames. Through this process, an absorption line at 1547.8 nm (in air at STP) was chosen that had no apparent interferences. All of the other acetylene transitions accessible with this laser showed water line interferences.

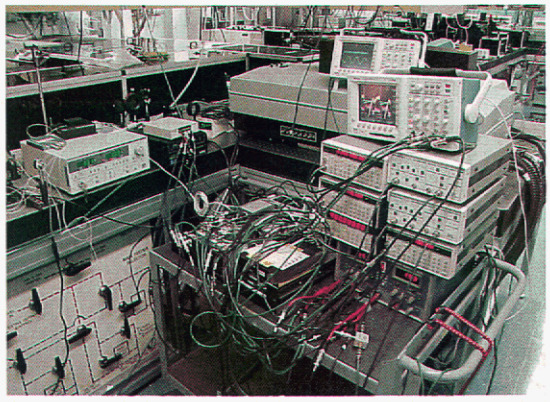

Figure 18. Photograph of TDLAS electronics setup: laser temperature controller to the left; function generators and lock-in amplifier electronics to the right.

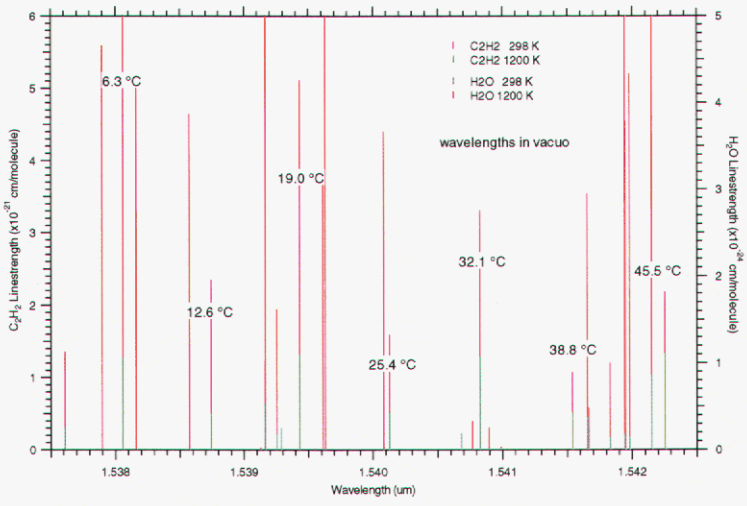

Figure 19. Linestrengths and line centers of water and acetylene absorption features within the tuning range of the diode laser used to measure acetylene. HiTran data is used for all but the high-temperature acetylene line strengths, which were derived from earlier spectral modeling (Shaddix et al., 2001). The temperatures indicate the laser control temperature used to produce laser light that is resonant with the indicated acetylene transition.

TDL measurements are notoriously sensitive to etalon effects from the laser beam passing through glass surfaces that are not anti-reflection (AR) coated or at least canted with respect to the axis of laser beam propagation. In the current application this was again found to hold true, as passage of the TDL beam through the window on either side of the burner chimney introduced etalon features in the recorded signals and passage of the beam through both windows introduced extremely large etalon features. Consequently, an AR-coated fiber optic pigtailed aspherical collimating lens was used to project the beam directly through the flame (see Fig. 20). On the opposite side of the flame, a strongly canted window was sealed to a piece of tubing that was itself press-sealed against the window, with a bore through the window. Once past the canted window, a focusing mirror brought the transmitted beam onto an InGaAs diode detector, thereby

reducing sensitivity to transient beam steering effects in the pulsed flames. 1310 nm and 1550 nm bandpass filters were used to attenuate broadband emission signals from the flames.

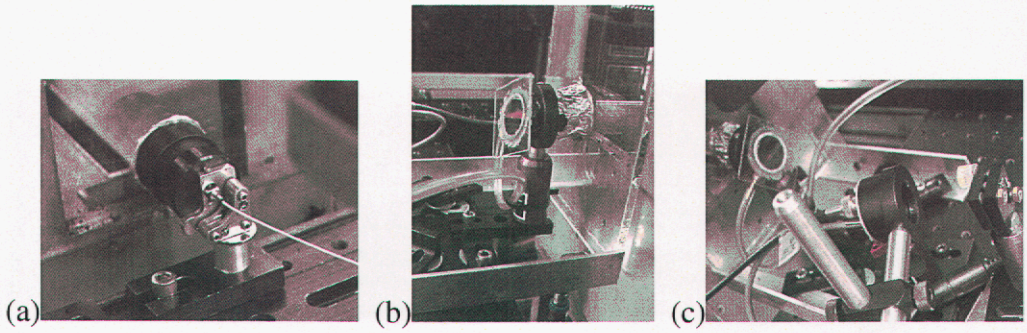

Figure 20. Photographs of TDLAS optical configuration, with (a) fiber pigtailed collimator within window-sealed body, (b) canted optical flat attached to window-sealed body, and (c) focusing mirror, bandpass filter, and diode detector, downstream of optical flat.

Figure 21 shows sample signals from a single wavelength sweep of the water laser. Signals were collected in 250 Hz spectral sweeps of the laser for steady flames and 900 Hz sweeps for pulsed flames, giving a phase resolution of 6° for the 15 Hz flames. The wavelength modulation spectroscopy was achieved using sinusoidal modulation at 1.1 MHz and lock-in detection at 2.2 MHz with a 8 μs time constant. One lock-in channel was nominally phase-locked for optimal signal strength, while the other was set at a 90° phase offset (providing data collection in quadrature). Signals were collected over several pulse cycles, allowing for subsequent averaging to improve signal-to-noise. Data were collected in 1 mm transverse steps across the slot flames at increments of 5 mm in height. The TDL beam through the flame was estimated to be 2 mm in diameter.

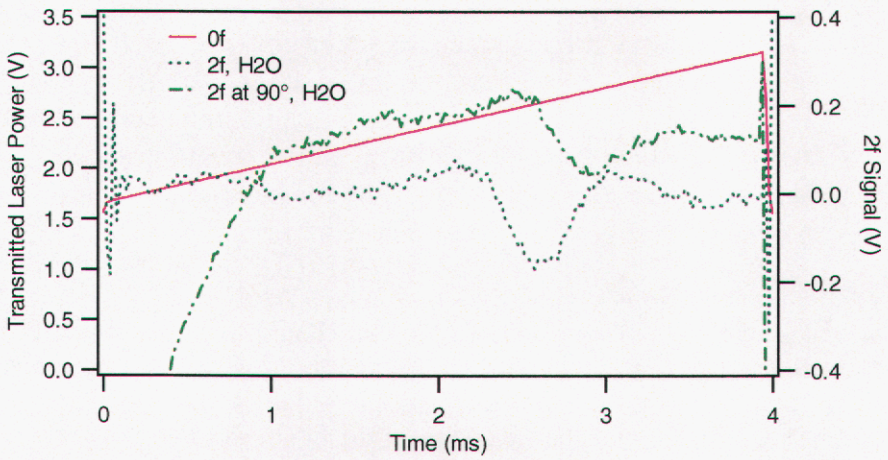

Figure 21. Example of a single 250 Hz ramp scan of a water absorption line at a height of 20 mm and a transverse position of 10 mm from the centerline of the steady ethylene slot flame. The two "2f" signals shown here are in a quadrature phase relationship.

Soot Dimensionless Extinction Coefficient

The dimensionless extinction coefficient of soot within the flames was measured using the transportable TCRN assembly originally constructed in Albuquerque, New Mexico, as part of a measurement campaign in large pool fires (Jensen et al., 2004). This device takes a sample stream containing soot, dilutes it, flows it through a 1-m long optical tube to allow accurate extinction measurements to be performed, and then allows a portion of the flow to be filtered for determination of the entrained soot mass. The existing design measures light extinction at both 635 nm and 1310 nm, thereby allowing determination of the dimensionless extinction coefficient, K_e, at both of these wavelengths. For this project, extensive modifications in the sampling configuration were necessary to minimize perturbation of the laminar flames by the sample probe. A tapered quartz microprobe was designed and constructed, based on a design previously used by researchers at Penn State University to sample gases from sooty methane and ethylene laminar diffusion flames (Puri, 1992; Kennedy et al., 1996) – see Fig. 22. The key operational feature of this probe is a solenoid driven wire that protrudes through the tip of the probe to prevent tip pluggage by soot. In practice, we found that in both our ethylene slot flame and kerosene coannular flame, excessive buildup of soot and tar occurred within the probe, on the solenoid activated wire, and on the outside of the probe. These deposits resulted in a strongly time-dependent soot sampling efficiency and severe perturbation of the flame flowfield.

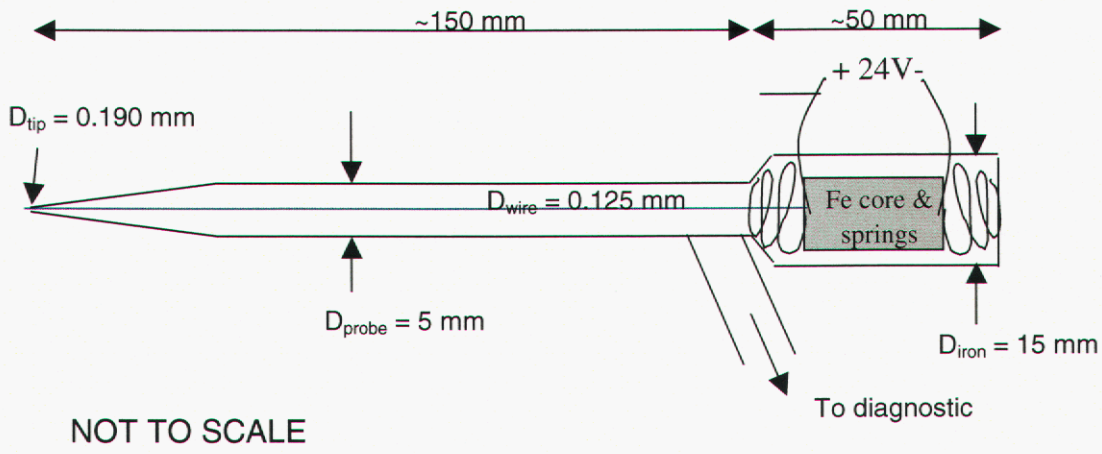

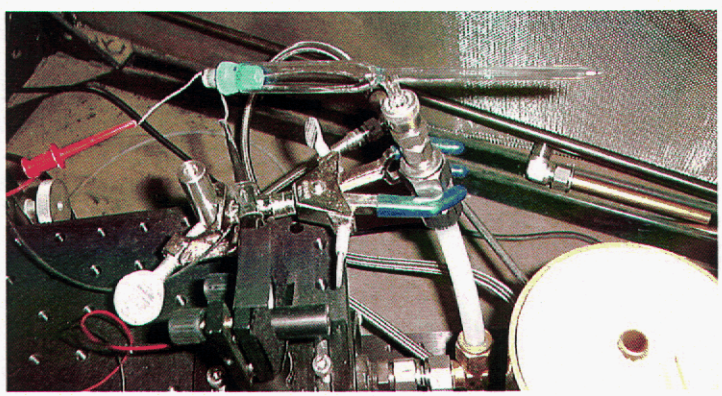

Figure 22. Schematic and photograph of quartz microprobe, constructed for unobtrusive soot sampling from laminar flames.

To surmount the problems encountered with the quartz microprobe, we tried sampling through straight-cut steel tubing and found that for a 1/8" stainless steel tube (3.175 mm OD, 1.75 mm ID) we could sample in the sootier flames without excessive buildup on the exterior of the probe. Further, by restricting the sample flow rate to 0.1 slpm, the probe had no noticeable effect on the *local* flame structure (*downstream* of the probe, the flame was obviously influenced – see Fig. 23). Soot buildup did occur inside the tube when sampling regions with high soot density, but we found that this flow restriction could be conveniently removed with a rapid backflush of the dilution nitrogen (5 slpm) out the end of the probe.

(a) 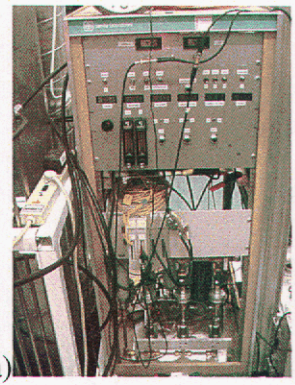 (b) 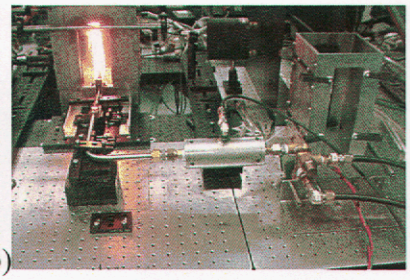 (c) 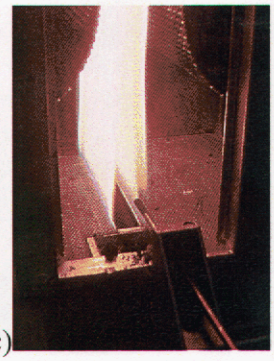

Figure 23. Photographs showing (a) equipment rack with flow controllers, valves, and filter assemblies for controlling operation of the TCRN, (b) soot transport and dilution line, leading from the flame, and (c) stainless steel sampling probe, drawing soot from the ethylene slot flame.

The phenomena of soot probe clogging and nitrogen backflushing added a significant dynamic component to the laser attenuation signals collected in the TCRN measurement, as shown in Fig. 24. Traditionally, the dimensionless extinction coefficient, K_e, has been calculated by collecting soot mass during a period of steady laser attenuation and by applying the following equation, using average values of the laser attenuation:

$$K_e = \frac{-\lambda \rho_{soot} V_{gas} \ln\left(I/I_0\right)}{L m_{soot}} \quad , \tag{1}$$

which is readily derived from Bouguer's Law:

$$\frac{I}{I_0} = \exp\left(\frac{-f_v K_e L}{\lambda}\right) \quad . \tag{2}$$

For application to situations where the instantaneous light extinction (and soot mass being collected) is varying significantly with time, Eq. 1 is only valid each instant in time (i.e., for each recorded datapoint) and must be integrated over the entire time period in which soot mass is being collected. This is equivalent to applying Eq. 1 using the total soot mass and the mean of $\ln(I/I_0)$. Using this analysis technique, K_e could be accurately determined even for sampling conditions in which several nitrogen backflushes were necessary to keep the probe from clogging.

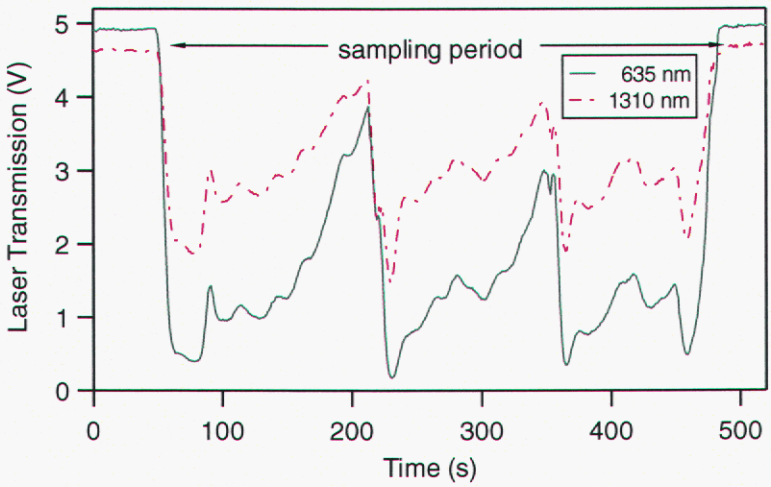

Figure 24. Time record of laser transmission signals from the TCRN diagnostic when sampling from the steady ethylene slot flame at a height of 65 mm. The plateau regions at the beginning and end of the time record denote the baseline laser transmission when the probe is sampling clean air. The two rapid drops in transmission in the middle of the sampling period follow probe backflushing events, temporarily allowing improved sampling of the soot.

Measurements of K_e were made at heights of 25 mm, 45 mm, and 65 mm in the steady methane and ethylene Wolfhard-Parker and coannular flames. In addition, a measurement was made at a height of 10 mm in the steady ethylene Wolfhard-Parker flame. For the kerosene flame, with its shorter flame height, measurements were made at heights of 25 mm, 35 mm, and 45 mm. For the 15 Hz pulsed flames, measurements were made at a height of 45 mm. At most sampling locations, at least two measurements were performed to assess the reproducibility of the measurement. Also, at every sampling position the radial location was chosen to roughly maximize the amount of soot being sampled. The spatial resolution of the sampling technique was deemed to be insufficient to effectively perform radial profiling through the thin soot layers. To optimize the consistency of the measurement in the different flames, the flowrates in the TCRN system were held constant throughout the series of measurements. Laminar flow elements were used to verify the indicated readings on the previously calibrated mass flow controllers. The collected soot masses varied from 0.4 mg to 4.3 mg, and these were determined by weighing teflon filters (with a weight of ~ 260 mg) before and after soot collection using a Mettler scale with a resolution of 0.01 mg. To verify the absence of any moisture condensation on the soot, several filters representing high and low derived K_e values were re-weighed after being placed in a dessicator for several days and showed no change of mass.

Figure 25 shows the measured values of K_e at 635 nm and 1310 nm as a function of height above the burner. The data are plotted in this manner because the height above burner acts as a surrogate for increasing soot residence time in the flame, and some variation of the soot optical properties may occur as the soot undergoes thermal annealing with increasing residence time at high temperatures (Shaddix et al., 2004-2). The results show that the fuel source and flame type both influence the value of K_e measured. Methane K_e values are generally lower than those for ethylene, which are in turn very similar to those of JP-8 (kerosene, not the JP-8 surrogate, was actually used for these measurements). The K_e values measured in the slot burner are generally lower than those from the coannular burner, especially at the near-infrared wavelength.

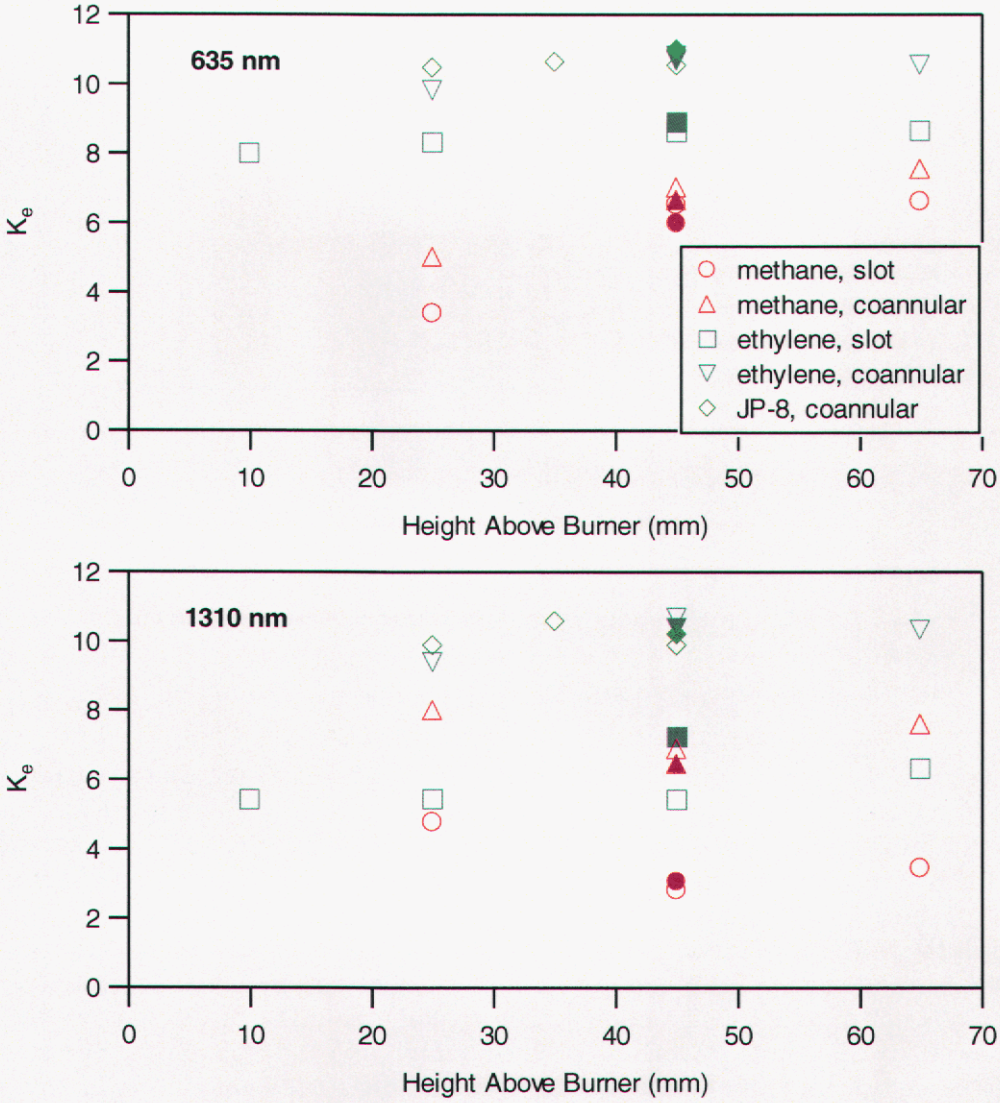

Figure 25. Dimensionless extinction coefficient of soot collected from the various flames investigated in this study. Filled symbols denote samples collected from pulsed flames operating at a 15 Hz pulsing frequency. Results from the 635 nm laser source are shown in the upper plot and results from the 1310 nm laser source are shown in the lower plot.

Recent measurements of K_e from overfire soot have yielded values between 8 and 10, in the same range as the coannular ethylene and JP-8 flame soot measured here. Measurements of soot extracted from the flame zone of large JP-8 pool fires (most likely a mixture of overfire and in-flame soot) yield K_e values between 7 and 10 for both 635 nm and 1310 nm, with a slight bias towards higher values at 635 nm (Jensen et al., 2004). No measurements of K_e for soot sampled directly from a laminar diffusion flame have been previously reported, nor have results of any kind from a methane-fueled flame been reported. For the conditions used in this study, the coannular flames have much more rapid heating of the interior region of the flame, in comparison to the Wolfhard-Parker flames. As a consequence, soot is formed more rapidly in the coannular flames and, based on the relative intensities of the PAH PLIF signals, PAH and tar

concentrations are lower. Therefore, the contribution of tar material to the collected soot mass would be expected to be lower in the case of coannular flames, consistent with the trend of higher K_e for these flames (tar does not tend to absorb light at visible and, especially, infrared wavelengths, so any inclusion of tar in the sampled mass reduces the derived K_e). Similarly, the low sooting propensity of methane results in a higher concentration of PAH and tar, relative to soot concentration, in these flames (Smyth et al., 1997), potentially explaining the low K_e values measured for methane flames. In fact, the methane soot samples have a distinct naphthalene ("mothballs") odor to them that is lacking in the kerosene and ethylene soot samples. We are currently pursuing the possibility of performing thermogravimetric analysis of the soot samples (measuring the rate of volatilization as a function of temperature) in order to evaluate the tar content of the collected samples.

Soot Microstructure

To measure the soot microstructure in these flames, a rapid insertion thermophoretic sampling system was designed and implemented for depositing soot particles onto exposed TEM grids. An initial design based on the large, rugged apparatus developed for sampling in pool fires was determined to be too slow and intrusive for sampling in our much smaller laminar flames. Consequently, we solicited the assistance of Prof. Constantine Megaridis of the University of Illinois at Chicago, who had invented this sampling technique while performing doctorate research at Brown University (Dobbins and Megaridis, 1987). Prof. Megaridis has subsequently improved the technique to make it as unobtrusive as possible. For this project, Prof. Megaridis visited Sandia and explained the details of the design and operation of his soot sampler. Subsequently, we designed a sampler based on his suggestions while accounting for the constraints of mounting and using such a sampler in our enclosed burner arrangements. A photograph of our sampler is shown in Fig. 26. In this design, a small pneumatic cylinder, powered by compressed air and a fast-acting solenoid valve, is used to drive a shaft forward and then backwards, with characteristic insertion and retraction times of 6 ms. The shaft ends with an attached metal shim that has a hole drilled in it for exposing a thin TEM grid that has been carefully inserted into the shim. Electronic control of the solenoid valve allows the "hold" time for sampling at the position of maximum extension to be set to any desired value. The extensional length is controlled by the travel length of the pneumatic cylinder. Transit times of the pneumatic cylinder were measured by passing two laser beams across the path of the tongue.

Typically, hold times on the order of 100 ms have been used when sampling soot from steady laminar flames. For sampling from our pulsed flames, we needed to use substantially shorter hold times, to prevent oxidation of the deposited soot when an oxidation zone passed by the flame sampling position during the flame pulse cycle. Consequently, we investigated the possibility of doing multiple exposures of the TEM grid into the flame (at the same phase timing of the pulse cycle) to build up the total exposure time and improve grid coverage by soot. A qualitative assessment suggested that the sampled soot structures indeed looked similar for multi-shot sampling in comparison to the traditional single-shot sampling, but we also found that reasonable soot aggregate collection could be achieved with as little as 10 ms exposure time in the ethylene slot flame. A sample TEM micrograph is shown as Fig. 27.

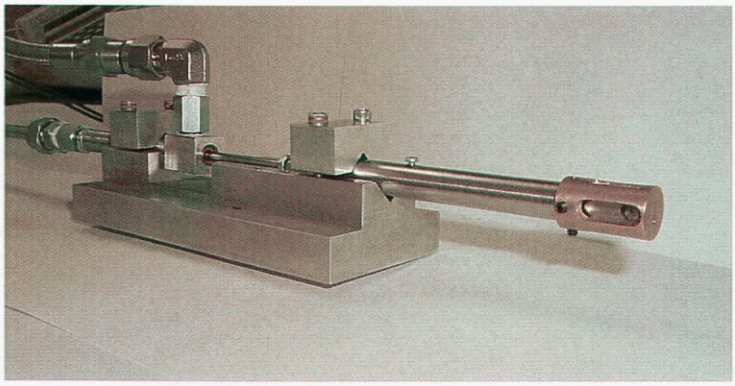

Figure 26. Photograph of thermophoretic sampler for collecting representative soot samples onto a TEM grid. Compressed air lines are attached to a pneumatic cylinder at the left of the photo. When activated, the cylinder drives a thin "tongue" containing the TEM grid through the slotted opening at the end of the brass cap (right). The cap acts to deflect sideways (away from the flame) the significant blast of air that is carried with the moving drive rod.

Figure 27. Sample TEM image of soot aggregates from the ethylene Wolfhard-Parker flame collected on a lacey grid.

One of the concerns of TEM grid sampling is the extent to which the flame structure is altered by the rapid insertion of the sampler tongue into the flame. This affect has been previously analyzed based on luminous imaging of the flame on a high-speed camera (Megaridis, 2002). This technique allows ready evaluation of the global effects of thermophoretic sampling on the flame, but does not provide explicit insight into any effects the tongue insertion may have on the flowfield inside the flamesheet. To evaluate this, the same OH and PAH PLIF technique described earlier in this report was applied with the laser sheet crossing the tip of the thermophoretic sampler tongue, when fully inserted into the flame. The resulting images are shown as Fig. 28. These images clearly show that the PAH layer, in particular, is affected by the insertion of the sampling tongue, but this effect is much more prominent downstream of the

sampling probe, which does not pose a concern for the integrity of the soot sampling itself. There is no evidence of significant perturbation of the soot-containing streamline upstream of the sampling position.

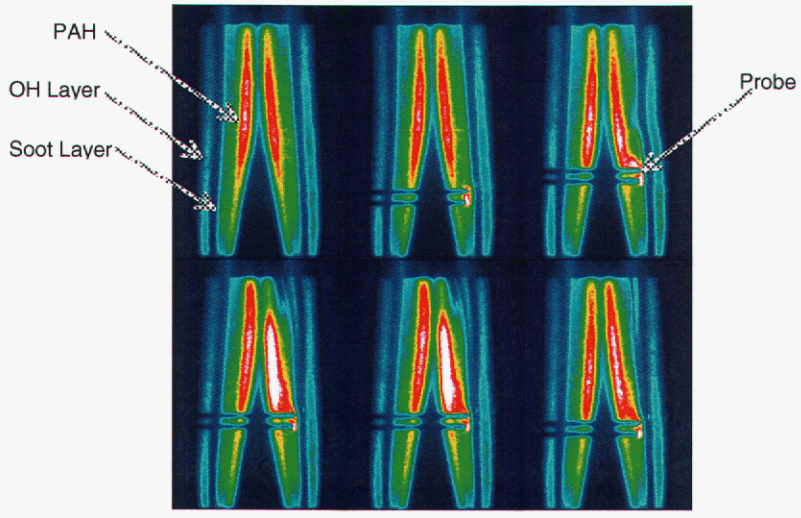

Figure 28. Simultaneously excited OH and PAH PLIF images of the steady ethylene Wolfhard-Parker flame with insertion of the thermophoretic sampler tongue into the flame. For this demonstration, the sampler operated with a 40 ms hold time. The tip of the sampler appears as a sharp scattering signal to the flame side of the right-hand PAH layer in each image. Laser light propagates from right-to-left in each image, revealing the shadowing effect of the sampler tongue tip.

Local Radiant Heat Flux

The local radiant heat flux from the flames was measured using a thin-film thermopile with a CaF_2 window and a 250 mm long sight tube with an ID of 2 mm. The sight tube was anodized to minimize light reflections. The use of the CaF_2 window material makes the radiometer equally sensitive to radiant emission from 0.13–11 μm, encompassing nearly all of the energy-containing radiation from the flame. The thermopile that was chosen for this measurement is 2 mm x 2 mm in size and has a characteristic response time of 85 ms. In theory, this response time is insufficient to fully resolve the dynamics associated with the pulsed flames that we investigated. However, we tried using faster responding thermopiles (smaller thermopiles and the same thermopile with a different bath gas) with time constants of 34 ms, 12.8 ms, and 5.6 ms, and found the measurement of the radiation dynamics from the 15 Hz ethylene slot flame to be precisely the same for the different thermopiles. Hence, we used the 85 ms thermopile for data collection because it gave the best signal-to-noise. Similarly, radial scans with the smaller thermopiles (1 mm x 1 mm and 0.9 mm x 0.4 mm) gave the same profile shape, so the 2 mm thermopile was deemed to be sufficiently small to maximize the spatial resolution in this setup. The radiometer was calibrated by mounting it in front of a high-temperature blackbody source (Fig. 29), whose display temperature was verified with a type R fine-wire thermocouple. The temperature of the thermopile was closely monitored during measurements and calibrations because of the sensitivity of the thermopile response to temperature. For measurements across sooty Wolfhard-Parker burner flames (which generate significant thermal radiation), thermal

conduction down the sight tube was found to result in heating of the thermopile, so a water jacket was formed around the sight tube and forced circulation of water from a temperature-controlled chiller was used to maintain the thermopile at the ambient lab temperature.

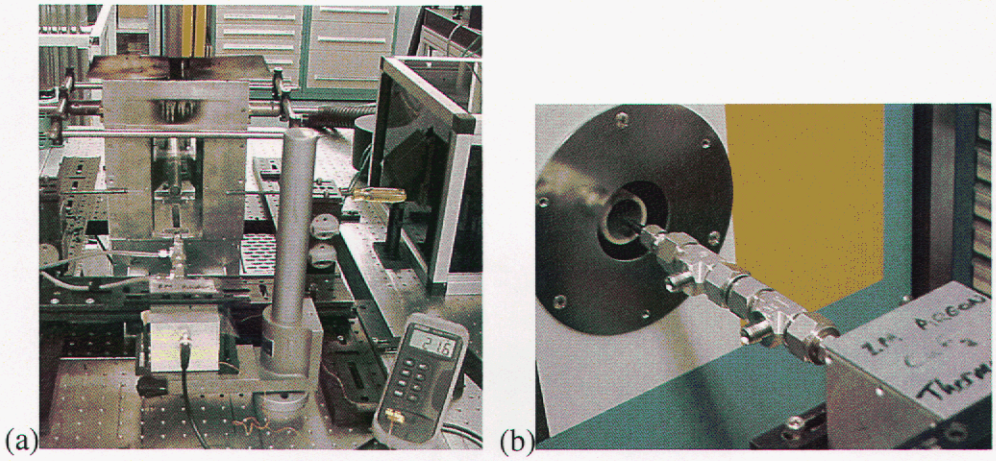

Figure 29. Photographs showing (a) experimental setup for radiometer measurements in the Wolfhard-Parker burner, and (b) setup for blackbody calibration of radiometer.

Radiometry measurements for the steady normal and inverse Wolfhard-Parker flames are shown in Fig. 30. These measurements show slightly greater total radiant emission from the normal slot flames in comparison to the inverse flames. Measurements of soot concentrations also showed somewhat lower values in the slot flames. The minor difference (factor of two) in total radiation from the methane and ethylene flames reflects the relatively low concentrations of soot in these flames (thereby allowing gas-phase radiation to play an important role) as well as the lower temperature of the soot in the ethylene flames. The soot concentrations in the ethylene flame are 20 times higher than in the methane flame.

For measurements in the coannular flames, a shorter, 150 mm long sight tube was used to boost the strength of the weak radiometer signals. The use of the shorter sight tube reduces the spatial resolution of the measurement by providing a larger angle of acceptance to the thermopile, but this is not believed to have a significant effect for the coannular flames, where the flame is constrained to the center of the burner. To interpret the measured signals as local radiant emission (in the same way as for the slot burner results), the data must be deconvolved using optical tomography.

Figure 31 shows a sample of the radiometer measurements in a pulsed ethylene slot flame. The reproducibility of the flame motion with the loudspeaker forcing of the fuel flow is clearly shown. From these measurements, the local, instantaneous radiant emission from the flames has been determined.

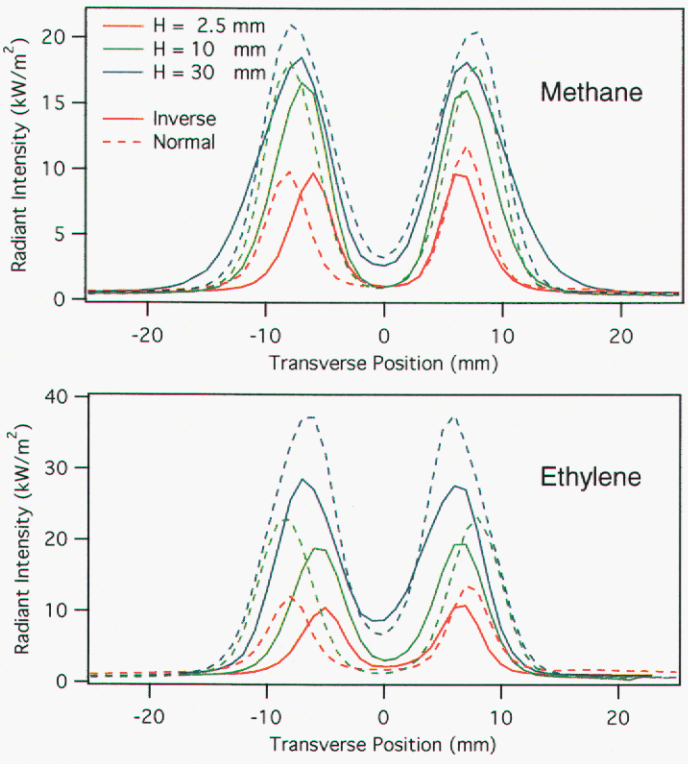

Figure 30. Radiometry measurements of the radiant emission profiles from steady normal and inverse slot flames.

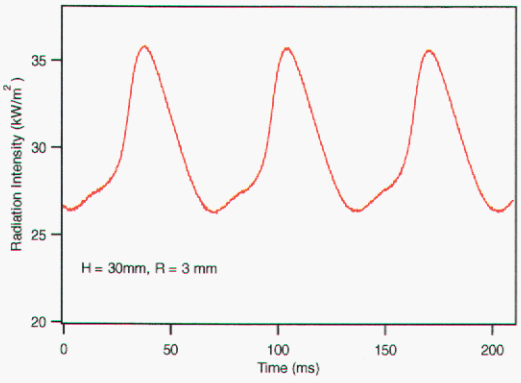

Figure 31. Time record of radiant emission from the 15 Hz pulsed ethylene slot flame at a height of 30 mm and a transverse position of 3 mm from the centerline.

Conclusions

In this LDRD project, several laser diagnostic techniques and extractive measurement techniques were employed in a series of laminar, soot-forming diffusion flames operating in both steady and pulsed, unsteady modes. The flames investigated included large Wolfhard-Parker flames of methane and ethylene burning in air and coannular flames of methane, ethylene, and a nitrogen-diluted JP-8 surrogate burning in air. In addition, partial characterization was performed of inverse Wolfhard-Parker (WP) flames of air burning in methane or ethylene. The measurement techniques that were employed in these flames included OH and PAH PLIF, near-IR radiation imaging, planar LII for soot concentration, PIV for velocity field, two-dimensional two-color pyrometry for temperature through the soot layer, TDLAS for water and acetylene concentrations (WP flames only), soot dimensionless extinction coefficient via a TCRN, soot microstructure (thermophoretic TEM grid sampling and analysis), and local radiant heat flux. Most of these techniques had been previously developed, but in nearly all cases adjustments had to be made to the means of implementing these techniques to make them work in sooty flames. As a consequence of the measurements performed in this project, a large quantity of high-quality data exists that can be synthesized and analyzed to provide new insights into the mechanisms and rates at which soot forms, grows, and oxidizes in diffusion flames, and also how it is transported and how much radiation it emits and absorbs. This is key information for the development of new constitutive models for large-scale, high-fidelity simulations of fire and also provides a unique database for validation of proposed models of soot formation, transport, and radiation in fires.

List of References

Agosta, A., Cernansky, N.P., Miller, D.L., Faravelli, T., and Ranzi, E. (2004), "Reference Components of Jet Fuels: Kinetic Modeling and Experimental Results," *Experimental Thermal Fluid Sci.* 28:701-708.

Cetegen, B.M., and Ahmed, T.A. (1993), *Comb. Flame* 93:157–184.

Dasch, C.J. (1992), "One-Dimensional Tomography: A Comparison of Abel, Onion-Peeling, and Filtered Backprojection Methods," *Appl. Optics* 31(8):1146-1152.

Dobbins, R.A., Fletcher, R.A., and Chang, H.-C. (1998), "The Evolution of Soot Precursor Particles in a Diffusion Flame," *Comb. Flame* 115:285-298.

Dobbins, R.A., Fletcher, R.A., and Lu, W. (1995), "Laser Microprobe Analysis of Soot Precursor Particles and Carbonaceous Soot," *Comb. Flame* 100:301-309.

Dobbins, R.A., and Megaridis, C.M. (1987), "Morphology of Flame Generated Soot as Determined by Thermophoretic Sampling," *Langmuir* 3(2):254-259.

Eddings, E.G., Yan, S., Ciro, W., and Sarofim, A.F., "Formulation of a Surrogate for the Simulation of Jet Fuel Pool Fires," submitted to *Combust. Sci. Tech.*

Edwards, T., and Maurice, L.Q. (2001), "Surrogate Mixtures to Represent Complex Aviation and Rocket Fuels," *J. Prop. Power* 17(2):461-466.

Gritzo, L.A., Gill, W., and Nicolette, V.F. (1998), "Estimates of the extent and character of the oxygen-starved interior in large pool fires," *Very Large Scale Fires, ASTM STP 1336* (N.R. Keltner, N.J. Alvares, and S.J. Grayson, Eds.), American Society for Testing and Materials, West Conshohocken, PA, 1998, pp. 84-98.

Hamins, A., Yang, J.C., and Kashiwagi, T. (1992), *Proc. Comb. Instit.* 24:1695–1702.

Hoffman, D., Münch, K.-U., and Leipertz, A. (1996), "Two-Dimensional Temperature Determination in Sooting Flames by Filtered Rayleigh Scattering," *Optics Letters* 21(7):525-527.

Jensen, K.A., Suo-Anttila, J.M., and Blevins, L.G., "Measurement of Soot Morphology, Chemistry, and Optical Properties in the Visible and Near-Infrared Spectrum in the Flame Zone and Overfire Region of Large JP-8 Pool Fires," submitted to *Comb. Flame.*

Kearney, S.P., Beresh, S.J., Schefer, R.W., and Grasser, T.W., "Filtered Rayleigh Scattering Diagnostic for Multi-Parameter Thermal-Fluids Measurements: LDRD Final Report," SAND2004-0158, Jan. 2004.

Kennedy, I.M. (1997), "Models of Soot Formation and Oxidation," *Prog. Energy Comb. Sci.* 23:95-132.

Kennedy, I.M., Yam, C., Rapp, D.C., and Santoro, R.J. (1996), "Modeling and Measurements of Soot and Species in a Laminar Diffusion Flame," *Comb. Flame* 107:368-382.

Leung, K.M., and Lindstedt, R.P. (1995), "Detailed Kinetic Modeling of C1—C3 Alkane Diffusion Flames," *Comb. Flame* 102:129-160.

Lindstedt, R.P., and Maurice, L.Q. (2000), "A Detailed Chemical Kinetic Model for Practical Aviation Fuels," *J. Prop. Power* 16(2):187-195.

McEnally, C.S., and Pfefferle, L.D. (1996), "Aromatic and Linear Hydrocarbon Concentration Measurements in a Non-Premixed Flame," *Combust. Sci. and Tech.* 116-117:183-209.

McEnally, C.S., and Pfefferle, L.D. (1998a), "Soot Formation in Methane/Air Non-Premixed Flames Doped with Small Quantities of C3 Hydrocarbons," *Comb. Flame* 112:545-558.

McEnally, C.S., and Pfefferle, L.D. (1998b), "Species and Soot Concentration Measurements in a Methane/Air Non-Premixed Flame Doped with C4 Hydrocarbons," *Comb. Flame* 115:81-92.

Megaridis, C.M., personal communication, June 2002.

Megaridis, C.M., and Dobbins, R.A. (1989), "Comparison of Soot Growth and Oxidation in Smoking and Non-Smoking Ethylene Diffusion Flames," *Combust. Sci. Tech.* 66:1-16.

Mitchell, R.E., Sarofim, A.F., and Clomburg, L.A. (1980), "Experimental and Numerical Investigation of Confined Laminar Diffusion Flames," *Comb. Flame* 37:227-244.

Mueller, C.J., and Schefer, R.W. (1998), "Coupling of Diffusion Flame Structure to an Unsteady Vortical Flow-Field," *Proc. Comb. Instit.* 27:1105-112.

Murphy, J.J., and Shaddix, C.R. (2004), "Influence of Scattering and Probe Volume Heterogeneity on Soot Measurements using Optical Pyrometry," *Comb. Flame*, in press.

Najm, H.N., Schefer, R.W., Milne, R.B., Mueller, C.J., Devine, K.D., and Kempka, S.N., "Numerical and Experimental Investigation of Vortical Flow-Flame Interaction," SAND98-8232, Feb. 1998.

Puri, Rahul, "The Interaction of Soot Particles with Carbon Monoxide in Laminar Diffusion Flames," PhD Thesis, Dept. of Mechanical Engineering, Penn State University, December 1992.

Puri, R., Moser, M., Santoro, R.J., and Smyth, K.C. (1992), "Laser-induced Fluorescence Measurements of OH· Concentrations in the Oxidation Region of Laminar, Hydrocarbon Diffusion Flames," *Proc. Comb. Instit.* 24:1015-1022.

Puri, R., Richardson, T.F., Santoro, R.J., and Dobbins, R.A. (1993), "Aerosol Dynamic Processes of Soot Aggregates in a Laminar Ethene Diffusion Flame," *Comb. Flame* 92:320-333.

Puri, R., Santoro, R.J., and Smyth, K.C. (1994), "The Oxidation of Soot and Carbon Monoxide in Hydrocarbon Diffusion Flames," *Comb. Flame* 97:125-144; and Erratum (1995), *Comb. Flame* 102:226-228.

Roper, F.G. (1977), "The Prediction of Laminar Jet Diffusion Flame Sizes: Part I. Theoretical Model," *Comb. Flame* 29:219–226.

Rothman, L.S., Rinsland, C.P., Goldman, A., Massie, S.T., Edwards, D.P., Flaud, J.-M., Perrin, A., Camy-Peyret, C., Dana, V., Mandin, J.-Y., Schroeder, J., McCann, A., Gamache, R.R., Wattson, R.B., Yoshino, K., Chance, K.V., Jucks, K.W., Brown, L.R., Nemtchinov, V., and Varanasi, P. (1998), "The HiTran Molecular Spectroscopic Database and HAWKS (HiTran Atmospheric Workstation): 1996 Edition," *J. Quant. Spectrosc. Radiat. Transfer* 60:665-710.

Santoro, R.J., Semerjian, H.G., and Dobbins, R.A. (1983), "Soot Particle Measurements in Diffusion Flames," *Comb. Flame* 51:203-218.

Santoro, R.J., and Semerjian, H.G. (1984), "Soot Formation in Diffusion Flames: Flow Rate, Fuel Species and Temperature Effects," *Proc. Comb. Instit.* 20:997-1006.

Santoro, R.J., and Shaddix, C.R., "Laser-Induced Incandescence," pp. 252-286, in Applied Combustion Diagnostics, (K. Kohse-Höinghaus and J.B. Jeffries, Eds.), Taylor and Francis, New York, 2002.

Santoro, R.J., Yeh, T.T., and Semerjian, H.G. (1987), "The Transport and Growth of Soot Particles in Laminar Diffusion Flames," *Combust. Sci. Tech.* 53:89-115.

Schefer, R.W. (1997), "Flame Sheet Imaging Using CH Chemiluminescence," *Combust. Sci. Tech.* 126:255–270.

Shaddix, C.R., Allendorf, S.W., Hubbard, G.L., Ottesen, D.K., and Gritzo, L.A., "Diode Laser Diagnostics for Gas Species and Soot in Large Fires: LDRD Project Final Report," Sandia National Labs Internal Report, SAND2001-8383, June 2001.

Shaddix, C.R., Harrington, J.E, and Smyth, K.C. (1994), "Quantitative Measurements of Enhanced Soot Production in a Flickering Methane/Air Diffusion Flames," *Comb. Flame* 99:723-732.

Shaddix, C.R., Palotás, Á.B., Megaridis, C.M., Choi, M.Y., and Yang, N.Y.C. (2004-2), "Soot Graphitic Order in Laminar Diffusion Flames and a Large-Scale JP-8 Pool Fire," submitted to *Int. J. Heat Mass Transfer.*

Shaddix, C.R., and Smyth, K.C. (1996), "Laser-Induced Incandescence Measurements of Soot Production in Steady and Flickering Methane, Propane, and Ethylene Diffusion Flames," *Comb. Flame* 107:418-452.

Shaddix, C.R., Williams, T.C., Blevins, L.G., and Schefer, R.W. (2004-1), "Flame Structure of Steady and Pulsed Sooting Inverse Jet Diffusion Flames," in press, *Proceedings of the Comb. Institute*, Vol. 30.

Smooke, M.D., McEnally, C.S., Pfefferle, L.D., Hall, R.J., and Colket, M.B. (1999), "Computational and Experimental Study of Soot Formation in a Coflow, Laminar Diffusion Flame," *Comb. Flame* 117:117-139.

Smyth, K.C., Harrington, J.E., Johnsson, E.L., and Pitts, W.M. (1993), "Greatly Enhanced Soot Scattering in Flickering CH4/Air Diffusion Flames," *Comb. Flame* 95:229-239.

Smyth, K.C., Shaddix, C.R., and Everest, D.A. (1997), "Aspects of Soot Dynamics as Revealed by Measurements of Broadband Fluorescence and Flame Luminosity in Flickering Diffusion Flames," *Comb. Flame* 111:185-207.

Snelling, D.R., Thomson, K.A., Smallwood, G.J., Gülder, Ö.L., Weckman, E.J., and Fraser, R.A. (2002), "Spectrally Resolved Measurement of Flame Radiation to Determine Soot Temperature and Concentration," *AIAA J.* 40(9):1789-1795.

Thuillard, M. (2002), *Fire Safety J.* 37:371–380.

Violi, A., Yan, S., Eddings, E.G., Sarofim, A.F., Granata, S., Faravelli, T., Ranzi, E. (2002), "Experimental Formulation and Kinetic Model for JP-8 Surrogate Mixtures," *Combust. Sci. Tech.* 174:399-417.

Will, Stefan, personal communication, July 2001.

Williams, T.C., Shaddix, C.R., and Desgroux, P., "The Response of Pulsed, Buoyant Diffusion Flames to Forcing Frequency and Amplitude," Proceedings of the Third Joint Meeting of the US Sections of the Combustion Institute, Paper C10, University of Illinois at Chicago, Chicago IL, March 16–19, 2003.

Distribution

1 Professor Philip J. Smith
Dept. of Chemical and Fuels Engineering
3290 Merrill Engineering Building
50 South Central Campus Drive
The University of Utah
Salt Lake City, UT 84112-9203

1 Professor Mitch Smooke
Dept. of Mechanical Engineering
Yale University
15 Prospect Street
New Haven, CT 06520-8284

1 Dr. Linda G. Blevins
Program Director, Comb. and Plasma Systems
National Science Foundation
4201 Wilson Boulevard, Suite 525
Arlington, VA 22230

Sandia Distribution

1	MS 0123	D.L. Chavez (LDRD Office), 01011
1	MS 9054	W.J. McLean, 08300
1	MS 9054	D.R. Hardesty, 08360
1	MS 9052	J.O. Keller, 08367
5	MS 9052	C.R. Shaddix, 08367
5	MS 9052	T.C. Williams, 08367
1	MS 0825	W.L. Hermina, 09110
1	MS 0821	L.A. Gritzo, 09132
1	MS 1135	J.M. Suo-Anttila, 09132
1	MS 1135	K.A. Jensen, 09132
1	MS 1135	S.R. Tieszen, 09132
1	MS 1135	J.C. Hewson, 09132
1	MS 0834	S.P. Kearney, 09112
3	MS 9018	Central Technical Files, 08945-1
1	MS 0899	Technical Library, 09616
1	MS 9021	Classification Office, 8511 for Technical Library, MS 0899, 9616
		DOE / OSTI via URL

This page intentionally left blank.